

High Spectral Resolution X-ray Observations of the Evolved Supermassive Stellar Binary System η Carinae — Iron $K\alpha$ Band Profile Revealed with *XRISM*

XRISM COLLABORATION:

MARC AUDARD,¹ HISAMITSU AWAKI,² RALF BALLHAUSEN,^{3,4,5} AYA BAMBA,⁶ EHUD BEHAR,⁷
ROZENN BOISSAY-MALAUQUIN,^{8,4,5} LAURA BRENNEMAN,⁹ GREGORY V. BROWN,¹⁰
MICHAEL F. CORCORAN,^{11,4,5} LIA CORRALES,¹² ELISA COSTANTINI,¹³ RENATA CUMBEE,⁴
MARIA DIAZ TRIGO,¹⁴ CHRIS DONE,¹⁵ TADAYASU DOTANI,¹⁶ KEN EBISAWA,¹⁶ MEGAN E. ECKART,¹⁰
DOMINIQUE ECKERT,¹ SATOSHI EGUCHI,¹⁷ TERUAKI ENOTO,¹⁸ YUICHIRO EZOE,¹⁹ ADAM FOSTER,⁹
RYUICHI FUJIMOTO,¹⁶ YUTAKA FUJITA,¹⁹ YASUSHI FUKAZAWA,²⁰ KOTARO FUKUSHIMA,¹⁶
AKIHIRO FURUZAWA,²¹ LUIGI GALLO,²² JAVIER A. GARCÍA,^{4,23} EMI GOTO,²⁴ LIYI GU,¹³
MATTEO GUAINAZZI,²⁵ KOUICHI HAGINO,⁶ KENJI HAMAGUCHI,^{8,4,5} ISAMU HATSUKADE,²⁶
KATSUHIRO HAYASHI,¹⁶ TAKAYUKI HAYASHI,^{8,4,5} NATALIE HELL,¹⁰ EDMUND HODGES-KLUCK,⁴
ANN HORNSCHEMEIER,⁴ YUTO ICHINOHE,²⁷ SHUN INOUE,¹⁸ DAIKI ISHI,¹⁶ MANABU ISHIDA,¹⁶
YUKIKO ISHIHARA,²⁴ KUMI ISHIKAWA,¹⁹ YOSHITAKA ISHISAKI,¹⁹ FRANCISCO JUNQUEIRA,¹¹
JELLE KAASTRA,^{13,28} TIMOTHY KALLMAN,⁴ YOSHIAKI KANEMARU,¹⁶ ERIN KARA,²⁹
SATORU KATSUDA,³⁰ RICHARD L. KELLEY,⁴ CAROLINE A. KILBOURNE,⁴ SHUNJI KITAMOTO,³¹
SHOGO KOBAYASHI,³² TAKAYOSHI KOHMURA,³³ AYA KUBOTA,³⁴ MAURICE LEUTENEGGER,⁴
MICHAEL LOEWENSTEIN,^{3,4,5} YOSHITOMO MAEDA,¹⁶ MAXIM MARKEVITCH,⁴
HIRONORI MATSUMOTO,³⁵ KYOKO MATSUSHITA,³² DAN MCCAMMON,³⁶ BRIAN MCNAMARA,³⁷
FRANÇOIS MERNIER,³⁸ BERT VANDER MEULEN,²⁵ ERIC D. MILLER,²⁹ JON M. MILLER,¹²
IKUYUKI MITSUISHI,³⁹ ASCA MIYAMOTO,¹⁹ MISAKI MIZUMOTO,⁴⁰ TSUNEFUMI MIZUNO,⁴¹
KOJI MORI,²⁶ KOJI MUKAI,^{8,4,5} HIROSHI MURAKAMI,⁴² RICHARD MUSHOTZKY,³
HIROSHI NAKAJIMA,⁴³ KAZUHIRO NAKAZAWA,³⁹ JAN-UWE NESS,⁴⁴ KUMIKO NOBUKAWA,⁴⁵
MASAYOSHI NOBUKAWA,⁴⁶ HIROFUMI NODA,⁴⁷ HIROKAZU ODAKA,³⁵ SHOJI OGAWA,¹⁶
ANNA OGORZALEK,^{3,4,5} TAKASHI OKAJIMA,⁴ NAOMI OTA,⁴⁸ STEPHANE PALTANI,¹ ROBERT PETRE,⁴
PAUL PLUCINSKY,⁹ FREDERICK S. PORTER,⁴ KATJA POTTSCHMIDT,^{8,4,5} KOSUKE SATO,⁴⁹
TOSHIKI SATO,⁵⁰ MAKOTO SAWADA,³¹ HIROMI SETA,¹⁹ MEGUMI SHIDATSU,² AURORA SIMIONESCU,¹³
RANDALL SMITH,⁹ HIROMASA SUZUKI,²⁶ ANDREW SZYMKOWIAK,⁵¹ HIROMITSU TAKAHASHI,²⁰
MAI TAKEO,³⁰ TORU TAMAGAWA,²⁷ KEISUKE TAMURA,^{8,4,5} TAKAAKI TANAKA,⁵²
ATSUSHI TANIMOTO,⁵³ MAKOTO TASHIRO,^{30,16} YUKIKATSU TERADA,^{30,16} YUICHI TERASHIMA,²
YOHKO TSUBOI,²⁴ MASAHIRO TSUJIMOTO,¹⁶ HIROSHI TSUNEMI,³⁵ TAKESHI TSURU,¹⁸
AYŞEGÜL TÜMER,^{8,4,5} HIROYUKI UCHIDA,¹⁸ NAGOMI UCHIDA,¹⁶ YUUSUKE UCHIDA,³³
HIDEKI UCHIYAMA,⁵⁴ SHUTARO UEDA,⁵⁵ YOSHIHIRO UEDA,⁵⁶ SHINICHIRO UNO,⁵⁷ JACCO VINK,^{58,13}
SHIN WATANABE,¹⁶ BRIAN J. WILLIAMS,⁴ SATOSHI YAMADA,⁵⁹ SHINYA YAMADA,³¹
HIROYA YAMAGUCHI,¹⁶ KAZUTAKA YAMAOKA,³⁹ NORIKO YAMASAKI,¹⁶ MAKOTO YAMAUCHI,²⁶
SHIGEO YAMAUCHI,⁶⁰ TAHIR YAQOUB,^{8,4,5} TOMOKAGE YONEYAMA,²⁴ TESSEI YOSHIDA,¹⁶
MIHOKO YUKITA,^{61,4} AND IRINA ZHURAVLEVA⁶²

¹Department of Astronomy, University of Geneva, Versoix CH-1290, Switzerland

²Department of Physics, Ehime University, Ehime 790-8577, Japan

³Department of Astronomy, University of Maryland, College Park, MD 20742, USA

⁴NASA Goddard Space Flight Center, Greenbelt, MD 20771, USA

⁵Center for Research and Exploration in Space Science and Technology (CRESSST II), Greenbelt, MD 20771, USA

- ⁶*Department of Physics, University of Tokyo, Tokyo 113-0033, Japan*
- ⁷*Department of Physics, Technion, Technion City, Haifa 3200003, Israel*
- ⁸*Center for Space Sciences and Technology, University of Maryland, Baltimore County, Baltimore, MD, 21250 USA*
- ⁹*Center for Astrophysics — Harvard-Smithsonian, Cambridge, MA 02138, USA*
- ¹⁰*Lawrence Livermore National Laboratory, Livermore, CA 94550, USA*
- ¹¹*The Catholic University of America, 620 Michigan Avenue NE, Washington, DC 20064, USA*
- ¹²*Department of Astronomy, University of Michigan, Ann Arbor, MI 48109, USA*
- ¹³*SRON Netherlands Institute for Space Research, Leiden, The Netherlands*
- ¹⁴*ESO, Karl-Schwarzschild-Strasse 2, 85748, Garching bei München, Germany*
- ¹⁵*Centre for Extragalactic Astronomy, Department of Physics, University of Durham, Durham DH1 3LE, UK*
- ¹⁶*Institute of Space and Astronautical Science (ISAS), JAXA, Kanagawa 252-5210, Japan*
- ¹⁷*Department of Economics, Kumamoto Gakuen University, Kumamoto 862-8680 Japan*
- ¹⁸*Department of Physics, Kyoto University, Kyoto 606-8502, Japan*
- ¹⁹*Department of Physics, Tokyo Metropolitan University, Tokyo 192-0397, Japan*
- ²⁰*Department of Physics, Hiroshima University, Hiroshima 739-8526, Japan*
- ²¹*Department of Physics, Fujita Health University, Aichi 470-1192, Japan*
- ²²*Department of Astronomy and Physics, Saint Mary's University, Nova Scotia B3H 3C3, Canada*
- ²³*California Institute of Technology, Pasadena, CA 91125, USA*
- ²⁴*Department of Physics, Chuo University, Tokyo 112-8551, Japan*
- ²⁵*ESA European Space Research and Technology Centre, Keplerlaan 1, 2201 AZ Noordwijk, The Netherlands*
- ²⁶*Faculty of Engineering, University of Miyazaki, 1-1 Gakuen-Kibanadai-Nishi, Miyazaki, Miyazaki 889-2192, Japan*
- ²⁷*RIKEN Nishina Center, Saitama 351-0198, Japan*
- ²⁸*Leiden Observatory, University of Leiden, P.O. Box 9513, NL-2300 RA, Leiden, The Netherlands*
- ²⁹*Kavli Institute for Astrophysics and Space Research, Massachusetts Institute of Technology, MA 02139, USA*
- ³⁰*Department of Physics, Saitama University, Saitama 338-8570, Japan*
- ³¹*Department of Physics, Rikkyo University, Tokyo 171-8501, Japan*
- ³²*Faculty of Physics, Tokyo University of Science, Tokyo 162-8601, Japan*
- ³³*Faculty of Science and Technology, Tokyo University of Science, Chiba 278-8510, Japan*
- ³⁴*Department of Electronic Information Systems, Shibaura Institute of Technology, Saitama 337-8570, Japan*
- ³⁵*Department of Earth and Space Science, Osaka University, Osaka 560-0043, Japan*
- ³⁶*Department of Physics, University of Wisconsin, WI 53706, USA*
- ³⁷*Department of Physics & Astronomy, Waterloo Centre for Astrophysics, University of Waterloo, Ontario N2L 3G1, Canada*
- ³⁸*IRAP, CNRS, Université de Toulouse, CNES, UT3-UPS, Toulouse, France*
- ³⁹*Department of Physics, Nagoya University, Aichi 464-8602, Japan*
- ⁴⁰*Science Research Education Unit, University of Teacher Education Fukuoka, Fukuoka 811-4192, Japan*
- ⁴¹*Hiroshima Astrophysical Science Center, Hiroshima University, Hiroshima 739-8526, Japan*
- ⁴²*Department of Data Science, Tohoku Gakuin University, Miyagi 984-8588*
- ⁴³*College of Science and Engineering, Kanto Gakuin University, Kanagawa 236-8501, Japan*
- ⁴⁴*ESA European Space Astronomy Centre, E-28692 Madrid, Spain*
- ⁴⁵*Department of Science, Faculty of Science and Engineering, KINDAI University, Osaka 577-8502, Japan*
- ⁴⁶*Department of Teacher Training and School Education, Nara University of Education, Nara 630-8528, Japan*
- ⁴⁷*Astronomical Institute, Tohoku University, Miyagi 980-8578, Japan*
- ⁴⁸*Department of Physics, Nara Women's University, Nara 630-8506, Japan*
- ⁴⁹*Department of Astrophysics and Atmospheric Sciences, Kyoto Sangyo University, Kyoto 603-8555, Japan*
- ⁵⁰*School of Science and Technology, Meiji University, Kanagawa, 214-8571, Japan*
- ⁵¹*Yale Center for Astronomy and Astrophysics, Yale University, CT 06520-8121, USA*

⁵²*Department of Physics, Konan University, Hyogo 658-8501, Japan*

⁵³*Graduate School of Science and Engineering, Kagoshima University, Kagoshima, 890-8580, Japan*

⁵⁴*Faculty of Education, Shizuoka University, Shizuoka 422-8529, Japan*

⁵⁵*Kanazawa University, Kanazawa, 920-1192 Japan*

⁵⁶*Department of Astronomy, Kyoto University, Kyoto 606-8502, Japan*

⁵⁷*Nihon Fukushi University, Shizuoka 422-8529, Japan*

⁵⁸*Anton Pannekoek Institute, the University of Amsterdam, Postbus 942491090 GE Amsterdam, The Netherlands*

⁵⁹*Frontier Research Institute for Interdisciplinary Sciences, Tohoku University, Sendai 980-8578, Japan*

⁶⁰*Department of Physics, Faculty of Science, Nara Women's University, Nara 630-8506, Japan*

⁶¹*Johns Hopkins University, MD 21218, USA*

⁶²*Department of Astronomy and Astrophysics, University of Chicago, Chicago, IL 60637, USA*

ABSTRACT

The supermassive binary system, η Carinae, is experiencing enormous wind-driven mass loss at a rate unparalleled in the rest of the Galaxy. Their wind-wind collision (WWC) continuously produces shock heated, X-ray emitting plasmas. The *XRISM* X-ray observatory observed the system in 2023 and 2024 when the X-ray emission began to increase toward periastron passage in 2025. This manuscript reports unprecedentedly high-resolution X-ray spectra in the iron $K\alpha$ band between 6.2 and 7.1 keV, obtained with the *Resolve* X-ray microcalorimeter. The hydrogen-like ($\text{Ly}\alpha$) and helium-like ($\text{He}\alpha$) lines reveal three velocity components. Two of them are broadened with maximum velocities of 2000–3000 km s⁻¹, likely originating from the post-shock companion wind. The other is relatively narrow, with a Gaussian broadening of only ~ 290 km s⁻¹ in 1 sigma, which may originate from the post-shock companion wind at the WWC stagnation point or penetrating the primary wind. The iron fluorescent lines exhibit a moderate blueshift and broadening with velocities at 100–200 km s⁻¹, consistent with the primary wind's velocity field. The spectra also confirm a Compton shoulder of the $\text{He}\alpha$ line complex for the first time. Both fluorescing and scattering spectral profiles indicate that the binary system is seen from the companion side during these observations. The flux ratio of the Compton scattering emission to the fluorescent line suggests substantial hydrogen depletion of the primary wind, expected from CNO-cycled hydrogen nuclear fusion gas.

Keywords: stars: abundances, stars: individual (η Carinae), stars: kinematics and dynamics, stars: massive, X-rays: stars

1. INTRODUCTION

Evolved massive stars lose a significant amount of mass through their winds (e.g., [Groh et al. 2014](#)). Their winds disperse nuclear-processed materials that emerge from the stellar interior to the surface, changing the circumstellar chemical composition. These processes mainly occur in the optical and infrared bands, but often evolve into high-energy phenomena as these stars tend to have a massive companion star, and their winds at a few thousand km s⁻¹ collide with each other. The wind-wind collision (WWC) produces a strong shock and thermalizes gas to an X-ray emitting temperature at

tens of millions of degrees Kelvin. Since X-ray observations provide the post-shock plasma conditions, and UV, optical, or infrared observations can provide information on the unshocked wind conditions (e.g., terminal velocity and mass loss rate), the WWC offers an ideal laboratory for studying astrophysical shock phenomena. The WWC X-rays also irradiate the surrounding materials, which then re-emit fluorescing or scattering X-rays. This provides an independent mean of probing the unshocked winds.

Theoretical studies suggest that the WWC occurs in a conical region where the momenta of two winds balance, and which wraps around the star with the weaker wind (Luo et al. 1990; Usov 1992; Stevens et al. 1992). Each hypersonic wind produces a shock, which heats post-shock gas in proportion to the square of the wind velocity, $kT \sim 2$ keV for $v = 1000$ km s⁻¹. When the shock is adiabatic, that is, the post-shock flow time is longer than the radiative cooling time, the post-shock plasma flows along the WWC contact discontinuity without significant cooling. In the opposite case, when the shock is radiative, the post-shock plasma collapses via quick cooling. In the adiabatic limit, the luminosity should scale inversely with the binary separation.

The evolved supermassive star η Carinae forms a binary system with another unseen massive companion, driving the most vigorous WWC activity in the solar neighborhood ($d \sim 2.35$ kpc, Daminieli 1996; Ishibashi et al. 1999; Smith 2006). The primary star with an estimated mass at $\gtrsim 90 M_{\odot}$ currently flows an enhanced mass loss wind ($v_{wind} \sim 420$ km s⁻¹, $\dot{M} \sim 8.5 \times 10^{-4} M_{\odot} \text{ yr}^{-1}$, Davidson et al. 1995; Cox et al. 1995; Hillier et al. 2001; Groh et al. 2012). The star once experienced an extreme mass loss event called the Great Eruption in the 1840s, which ejected several tens of solar masses of nitrogen-rich materials, now seen as the bipolar Homunculus nebula (Morris et al. 2017; Smith et al. 2003). The star is thus classified as an unstable Luminous Blue Variable (LBV) phase. The historical ejecta and the current thick wind heavily obscure the companion. However, X-rays and optical monitoring observations of the star since the late 1990s have found periodic variations from the WWC plasma, revealing the presence of a massive companion star in a long, highly eccentric orbit ($P = 5.54$ year, $e \sim 0.9$, Daminieli et al. 2008; Corcoran et al. 2017; Espinoza-Galeas et al. 2022). The observed X-ray characteristics ($kT \sim 4$ keV, $L_X \sim 10^{35}$ ergs s⁻¹) indicate that the companion star has a relatively thin, fast wind ($v_{wind} \sim 3000$ km s⁻¹, $\dot{M} \sim 10^{-5} M_{\odot} \text{ yr}^{-1}$, Pittard & Corcoran 2002). These wind characteristics and high ionization UV and optical emission from reflection nebulae suggest that the companion is an O supergiant or nitrogen-rich Wolf-Rayet (WN) star (Verner et al. 2005; Mehner et al. 2010).

Because of its importance for understanding the stellar evolution and shock physics, η Carinae has been a frequent target of X-ray observatories (Corcoran et al. 1995; Tsuboi et al. 1997; Corcoran et al. 1998b, 1997; Ishibashi et al. 1999; Corcoran et al. 2000, 2001; Leutenegger et al. 2003; Behar et al. 2007; Hamaguchi et al. 2007; Henley et al. 2008; Leyder et al. 2008; Sekiguchi et al. 2009; Leyder et al. 2010; Hamaguchi et al. 2014a,b, 2016; Corcoran et al. 2017; Hamaguchi et al. 2018; Kashi et al. 2021; Espinoza-Galeas et al. 2022). Among them, the *Chandra* Observatory's High-Energy Transmission Grating Spectrometer (HETGS) provided the highest resolution η Carinae spectra, which clearly separated emission lines from highly ionized Mg, Si, S, and Ca ions (Corcoran et al. 2001; Behar et al. 2007; Henley et al. 2008; Espinoza-Galeas et al. 2022). The Si and S emission lines exhibited strong blue-shifted tails up to ~ 2000 km s⁻¹, which evolved as the binary system approached periastron (Behar et al. 2007). Their line centroids also vary with the orbit motion,

which, however, cannot be reproduced with simple geometrical models, in which the post-shock plasma flows constantly from the apex on a conical surface (Henley et al. 2008).

The Fe He α and Ly α emission lines between 6–7 keV trace η Carinae’s hottest WWC plasma near the apex, which should provide crucial information on the WWC shock physics. Unfortunately, *Chandra*/HETGS has limited energy resolution (~ 30 eV) and collecting area (~ 30 cm²) at 6 keV⁶³, barely resolving the Fe He α line complex and the fluorescent K α line (e.g., Corcoran et al. 2001). *XRISM/Resolve* features a superb energy resolution of ~ 4.5 eV and a collecting area of ~ 180 cm² at 6 keV (Tashiro et al. 2025). The *Resolve* spectra of η Carinae reveal multiple velocity components in the iron emission lines as well as faint but important spectral features, such as the Compton shoulders and absorption edges, in unprecedented detail. This paper reports the results of the initial *XRISM* observations of η Carinae, conducted during the observatory’s commissioning phase in 2023 and performance verification phase in 2024.

2. OBSERVATIONS & DATA REDUCTION

The *XRISM* X-ray observatory was launched from the Tanegashima Space Center in Japan on September 6, 2023 (UTC). It has two X-ray telescopes, *Resolve* and *Xtend*, each comprising an X-ray Mirror Assembly (XMA) and a focal plane X-ray instrument (Tashiro et al. 2025). The XMA of the two telescopes are nearly identical (Hayashi et al. 2024). Each XMA employs conically approximated Wolter I optics with 203 nested shells, focusing X-rays in a point-spread function (PSF) with a half-power diameter of 1.3’–1.4’. *Resolve*’s focal plane instrument is an X-ray microcalorimeter array, comprising 35 pixels of 30’’ \times 30’’ each with a total field of view (FOV) of 3.1’ \times 3.1’ (Kelley 2024). The detector is operated at 50 milli-Kelvin to detect a slight temperature increase by absorption of an X-ray photon. This technology enables a superb energy resolution of ~ 4.5 eV at 6 keV with High-resolution Primary (Hp) events, each of which does not have another event within 70.7 milliseconds. *Resolve* is designed to be sensitive between 0.3–12 keV. However, the detector gate valve used to keep a vacuum during launch had not successfully opened in orbit, limiting sensitivity during these observations to X-ray energies above 1.7 keV and reducing the collecting area to $\sim 60\%$ of the area with the gate valve opened at 6 keV (Porter et al. 2024). *Xtend*’s focal-plane instrument is an X-ray CCD camera with four identical CCD chips aligned squarely, covering a wide 38.5’ \times 38.5’ field of view (Mori et al. 2024). The CCD chips employ backside-illuminated, p-channel technology, which enables high quantum efficiency between 0.4–13 keV. The aim point is approximately 4.7’ from the two inner chip edges on CCD_ID =1, so that the main target is not placed on a chip gap. The CCDs nominally take a frame exposure every 4 seconds. However, two CCDs, CCD_ID =0 & 1 can continuously read only one-eighth of the field of view every 0.5 second, in order to avoid photon pileup for bright sources and/or increase the time resolution.

XRISM observed η Carinae twice, starting on 2023 November 23 at the binary orbital phase $\phi_X = 0.68$ during the observatory’s commissioning phase and on 2024 June 9 at $\phi_X = 0.78$ during the performance verification phase, where the binary ephemeris is from Corcoran et al. (2017) equation 4 (the cycle count $E = \phi_X + 4.0$ for these observations, see also Table 1 and Figure 1). Hereafter, we abbreviate each observation with the last 2 digit of the year, two digits for the month, and the date, each after XRI, e.g., XRI231123 for the 2023 observation, XRI240609 for the 2024 observation. XRI231123 was conducted for telescope pointing calibration without *Resolve* gain data acquisition

⁶³ <https://cxc.harvard.edu/proposer/POG/html/chap8.html>

Table 1. Log of the *XRISM Resolve* Observations

Obs.	Obs. ID	Start/Stop Time		Phase	Duration (ksec)	Exposure (ksec)	CR (cnts s ⁻¹)	v_{\oplus} (km s ⁻¹)
		Time	Time					
231123	000121000	2023 Nov. 23 02:06 ...	24 03:00	4.6811...6	89.7	44.2	0.76	9.8
240609	300067010	2024 June 9 01:17 ...	13 07:41	4.7794...815	368.7	296.0	1.1	-12.8

NOTE— Start/Stop Time: time interval with *Resolve* data after the standard screening.

Phase: binary orbital phase derived from the ephemeris in [Corcoran et al. \(2017\)](#) equation 4.

CR: *Resolve* Hp count rate between 1.7–12.0 keV.

v_{\oplus} : barycentric radial velocity of the Earth to η Carinae, calculated with the `radial_velocity_correction` method in the `SkyCoord` class of the `astropy` coordinates package. The positive sign is when the Earth is moving toward the star.

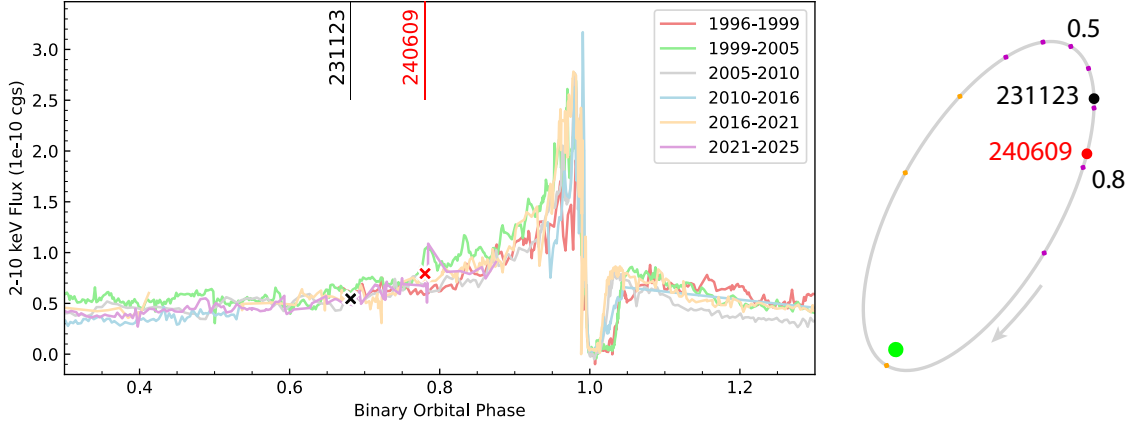


Figure 1. *Left:* *XRISM* η Carinae observations in the 2–10 keV flux modulation plot folded with the binary orbital period, obtained with *RXTE*, *Swift*, and *NICER* since 1996 (Corcoran et al. 2017; Espinoza-Galeas et al. 2022, — a complete analysis, including *NICER* data obtained after 2021, will be presented in a forthcoming manuscript.) The crosses show the 2–10 keV fluxes during the *XRISM* observations (black: XRI231123, red: XRI240609), which are similar to those observed during earlier epochs near their orbital phases. *Right:* Companion star’s locations in a binary orbit during the *XRISM* observations.

during the observation (see Appendix A for details). The data without proper calibration leaves a ~ 20 eV absolute gain offset and an additional instrumental broadening. The *Resolve* instrument team made a special gain calibration of the data using ^{55}Fe gain calibration obtained during the previous observation, which improves the spectral gain accuracy to $\lesssim 1$ eV. XRI240609 was performed with an efficient gain calibration, achieving a gain accuracy of $\lesssim 0.1$ eV (Porter et al. 2024). *Xtend* used the one-eighth window option for XRI231123 and the full window option for XRI240609. The latter dataset suffered from significant pileup near the PSF core of η Carinae, and therefore, we use *Xtend* data for checking potential contamination by nearby X-ray sources. XRI240606 *Xtend* observation detected a moderate X-ray flare from a young stellar object at $13.8'$ from η Carinae (Yoshida et al. 2024), which had no impact on the analysis of the *Resolve* spectrum. Otherwise, no source in the *Xtend* FOV significantly contaminated the *Resolve* η Carinae data.

We reprocessed the XRI240609 data with `xpipeline` in HEASoft version 6.35.1, applying CALDB 20250315, while we use the XRI231123 *Resolve* data reprocessed by the *XRISM* data processing team with HEASoft version 6.34 and using the tailored gain history file (Appendix A). For both datasets, we followed the analysis instructions in the *XRISM* data reduction guide⁶⁴ version 1.0. We screened the data using standard criteria, selecting intervals above the geomagnetic cutoff rigidity indicator CORTIME above 4, which encompasses all good time intervals that meet the standard criteria. For the *Resolve* spectral analysis, we selected Hp-grade events with the highest energy resolution and exclude pixel-pixel coincident events. We produced spectra from all active pixels but pixel 27, which occasionally shows unpredictable gain variations. The Hp count rates of 34 pixels between 1.7–12 keV are 0.764 cts s^{-1} during XRI231123 and 1.11 cts s^{-1} during XRI240609. At these low *Resolve* count rates, almost all Low-resolution Secondary (Ls) events are expected to originate from

⁶⁴ https://heasarc.gsfc.nasa.gov/docs/xrism/analysis/abc_guide/xrism_abc.html

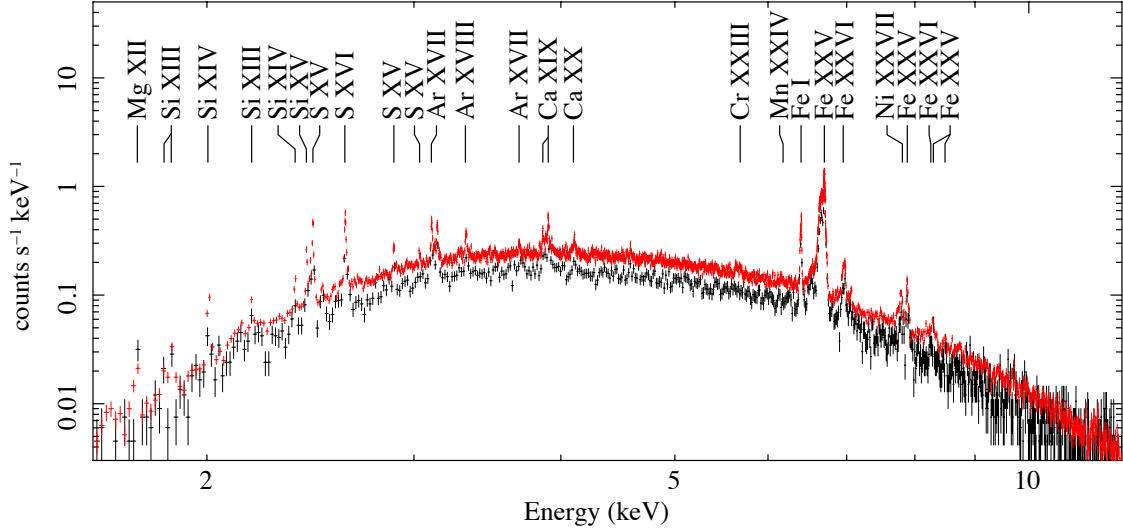


Figure 2. *Resolve* spectra of η Carinae during XRI231123 (black) and XRI240609 (red).

the particle background. We, therefore, excluded them in calculating the Hp event branching ratio for spectral response (`rmf`) production.

We evaluated the non-X-ray background (NXB) contribution in the *Resolve* data using `rslnxbgen` by following the procedure described in the “NXB Spectral Models” page⁶⁵. We extracted an Hp-grade background spectrum from version 2 of the night Earth database⁶⁶, obtained within ± 150 days of each observation, outside of the South Atlantic Anomaly passage, with Earth elevation less than -5° , Day Earth elevation more than 5° , and CORTIME above 4. We then fit the spectrum to the `v1` model (`rs1_nxb_model_v1.mo`) paired with the diagonal matrix, `newdiag60000.rmf`, using the X-ray fitting package `XSPEC` (Arnaud 1996). We added the best-fit NXB model to the source model for spectral fittings. The NXB spectrum in the Fe $K\alpha$ band includes very weak Fe fluorescent lines; however, the NXB contribution at any relevant energy range is less than 0.5% of the source spectrum. The cosmic-ray background (CXB) is $< 25\%$ of the NXB, so we ignored the CXB contribution.

3. RESULTS

XRI240609 is the longest observation of η Carinae with any sensitive X-ray focusing telescope. Nevertheless, η Carinae did not show any significant X-ray time variation during this observation. We produced a 1.7–12 keV *Resolve* light curve of the observation with 200-second time bins, each with more than 80% (160 sec) on-source time. A constant model reproduces the light curve very well with $\chi^2/\text{dof} = 1383.0/1450$, where dof is the degrees of freedom. XRI231123 similarly does not show significant variation with $\chi^2/\text{dof} = 222.8/207$. These results are similar to earlier X-ray observations of η Carinae, which do not show any short-term variation except near periastron (e.g., Hamaguchi et al. 2007, 2016).

Since η Carinae does not exhibit significant variation in either observation, we produced a spectrum from the entire dataset for each observation (Figure 2). The two spectra are very similar except for their fluxes: a simple model fit yields 2–10 keV fluxes of 5.5×10^{-11} ergs cm^{-2} s^{-1} for XRI231123 and

⁶⁵ https://heasarc.gsfc.nasa.gov/docs/xrism/analysis/nxb/nxb_spectral_models.html

⁶⁶ <https://heasarc.gsfc.nasa.gov/docs/xrism/analysis/nxb/index.html>

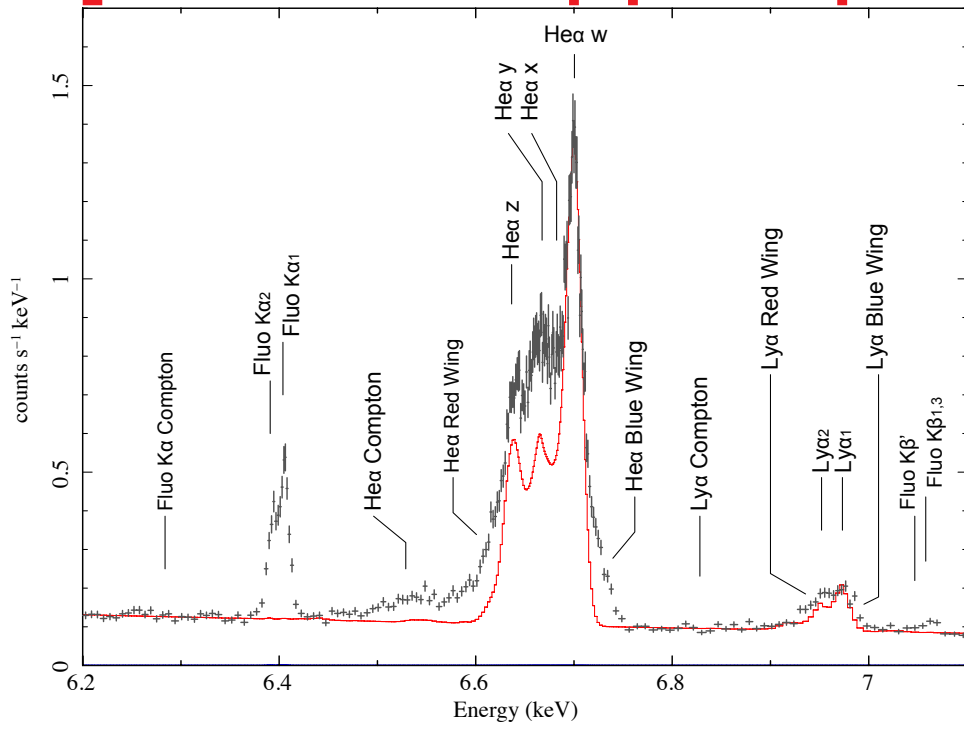


Figure 3. *Resolve* Fe $K\alpha$ band spectrum of η Carinae in XRI240609. The solid red line shows the best-fit optically thin, collisional equilibrium one-temperature thermal plasma (*bapec*) model derived from a fit to the data in the top red bar ranges. The blue line barely above the x-axis shows the estimated non-X-ray background spectrum.

7.9×10^{-11} ergs cm^{-2} s^{-1} for XRI240609. They exhibit strong line emission from highly ionized ions of multiple elements, Si, S, Ar, Ca, Fe and Ni. They also show minor enhancements at some energies, which may be emission lines of rare elements, such as Cr and Mn. These spectra are similar to earlier *Chandra* high-resolution spectra (e.g., Corcoran et al. 2001), but with significantly enhanced energy resolution and throughput. The *Resolve* spectra separated the emission lines and display their profiles in unprecedented detail.

This paper focuses on the spectral features between 6.2 and 7.1 keV, which contain several Fe $K\alpha$ lines from various ionization states (Figure 3). We scrutinized the XRI240609 spectrum, which has an order of magnitude higher photon statistics than XRI231123, and apply the result to XRI231123 for a comparison.

3.1. Iron $K\alpha$ Line Profile

The most conspicuous feature in this energy band is the Helium-like Fe $K\alpha$ (Fe He α) line complex between 6.6–6.7 keV. The narrow peak at ~ 6.70 keV corresponds to the resonance line (He α - w). It does not show a significant energy shift from the rest frame, but it is significantly broader than the instrumental broadening. The complex also has two peaks at ~ 6.665 keV and ~ 6.64 keV, which

correspond to the inter-combination lines ($\text{He}\alpha\text{-}y$) and the forbidden line ($\text{He}\alpha\text{-}z$) (e.g., [Porquet et al. 2010](#)). *Resolve* has enough spectral resolutions to separate these lines from each other, but the intrinsic Doppler broadening blends them. The broadening also should submerge weaker emission lines between them.

The spectrum also shows two weaker peaks at ~ 6.97 keV, which correspond to the Hydrogen-like Fe $\text{K}\alpha_1$ ($\text{Ly}\alpha_1$) and $\text{K}\alpha_2$ ($\text{Ly}\alpha_2$) lines. These lines are also heavily blended due to Doppler broadening. The relatively sharp line at ~ 6.40 keV corresponds to the fluorescent Fe $\text{K}\alpha$ line emission from quasi-neutral ionization states. It also appears to have two peaks, whose energy difference is consistent with the $\text{K}\alpha_1$ and $\text{K}\alpha_2$ emission lines. The spectrum also clearly shows a weak peak at ~ 7.06 keV, corresponding to the fluorescent iron $\text{K}\beta$ line emission.

The spectrum also reveals structures that are not recognized in conventional stellar X-ray spectral profiles. To highlight them, we compare the spectrum with a simple one-temperature plasma emission model, which satisfies the spectrum in the following four specific energy bands: Band *i*) 6.700 ± 0.05 keV, including the broadened $\text{He}\alpha$ resonance line; band *ii*) 6.973 ± 0.05 keV, covering the $\text{Ly}\alpha_1$ line peak; and bands *iii*) and *iv*) $6.2\text{--}6.22$ keV and $6.755\text{--}6.765$ keV dominated by electron-continuum emission without any strong emission lines. These bands are depicted as the red bars in [Figure 3](#). We fit these bands with a one-temperature velocity-broadened thermal plasma emission model (**bapec**). Band *i*) mainly constrains the redshift (z) and the broadening velocity (v_σ). The ratio of band *ii*) to band *i*) constrains the plasma temperature (kT). Bands *iii*) and *iv*) mainly constrain the continuum level — the **bapec** model normalization ($norm$). The ratio of the line flux over the continuum constrains the elemental abundance (Z). The best-fit parameters are kT : 3.97 keV, Z : 0.403 solar, z : 0.00, v_σ : 332 km s^{-1} , and $norm$: 0.126. The best-fit model is plotted in red in [Figure 3](#). We note that this model is designed to highlight the intrinsic spectral shape from the spectral response profile: the derived parameters, in particular the elemental abundance, should not necessarily reflect the actual plasma conditions.

The best-fit model reproduces the broadening of the resonance line profile fairly well. The plasma temperature, which mainly represents the characteristic ionization temperature of highly ionized Fe, is consistent with the slope above 7.1 keV, which traces the electron temperature, and similar to the typical hottest plasma temperatures of η Carinae’s WWC X-ray emission measured in earlier observations ([Hamaguchi et al. 2007, 2014b, 2016](#)). However, the model fails to reproduce the blue and red wings of both the $\text{He}\alpha$ and $\text{Ly}\alpha$ lines. Lithium-like dielectronic recombination (DR) lines from cooler plasma may explain a fraction of the $\text{He}\alpha$ red wing, but no emission line explains the other wing excesses. The model also explains only $\sim 60\%$ of the satellite line band flux between $6.63\text{--}6.69$ keV. Plasmas in collisional ionization equilibrium (CIE) at lower temperatures or non-equilibrium ionization (NEI) exhibit stronger emission in this band, but have a significantly weaker $\text{Ly}\alpha$ line. These results suggest the presence of additional thermal components with substantial Doppler broadening and/or other mechanism.

The $\text{He}\alpha$ red excess extends down to ~ 6.45 keV with a small peak at ~ 6.54 keV. To reproduce this excess by a Doppler-broadened $\text{He}\alpha$ Fe line would require a plasma velocity up to $v \approx 12000 \text{ km s}^{-1}$, which is much higher than those observed from η Carinae or wind from any other massive stellar system. On the other hand, cold materials that produce fluorescence Fe lines can also Compton-scatter X-ray emission via electron interaction. Compton scattering removes a fraction of the photon energy, depending on the scattering angle. $\text{He}\alpha\text{-}w$ photons at 6.70 keV down-scatter to 6.53 keV for

180° back-scattering, consistent with the observed local peak. The peak is not as clear as the source thermal spectrum, because of multiple-angle scattering emission. This excess emission should be the so-called Compton shoulder profile of the Fe He α line. This would be the first clear detection of a Compton shoulder profile associated with a thermal emission line, rather than the Fe K α fluorescence line. In the meantime, the spectrum also shows a marginal enhancement above the continuum below the fluorescent K α line down to the back-scattering energy at ~ 6.24 keV, suggesting a detection of the Compton shoulder of the Fe K α fluorescence line as well.

3.2. Spectral Fitting Model

Because the single-temperature model above provide a poor fit, we add two additional Doppler-broadened components for the blue and red wings, fluorescent iron K α and K β lines, and Compton scattering components for each thermal component and the fluorescent K α line to the one-temperature model. Hereafter, we call the initial `bapec` component, which reproduces the relatively narrow He α - w line, the “narrow” component and designate it as N .

A preliminary fit suggests that adding a single Gaussian broadened thermal component (`bapec`) can reproduce most of the blue and red wing excesses. However, lower-energy emission lines from Si, S, Ar, and Ca ions, which will be described in a subsequent paper, exhibit similar blue wings but significantly weaker or no red wings. This suggests that the two wings have different origins and should be treated separately. Reproducing a wing profile requires a smoothing only to one energy direction, but the standard `Xspec` library lacks such a convolution function. We therefore develop an empirical asymmetric smoothing function, `htsmooth`, which redistributes the flux in each spectral bin to a half-diagonal shape (Appendix B.1). For each wing component, we convolved this function to an `apec` model, whose temperature, abundance, and redshift parameters were tied to the corresponding parameters of the narrow component.

`Xspec` includes several Compton scattering models, which, however, assume a power-law source spectrum. We need a new model that considers down-scattering of thermal emission lines. Compton scattering spectra can change with multiple conditions: i) the emitting source’s spatial and velocity distribution; ii) the reflector’s spatial and velocity distribution; iii) the reflector’s density, elemental abundances, and ionization states; and iv) the orientation of the reflector to the observer. A complete reproduction of the Compton spectral shape requires a detailed modeling of the WWC geometry, which is beyond the scope of this paper. We therefore developed an empirical Compton down-scattering model, `emcomp` (Appendix B.2), which assumes a simple redistribution function within the Compton down-scattering energy range and varies the function parameters to fit the Compton scattering profile. The current version does not account for photoelectric absorption so it is only applicable to restricted bands with negligible variation in absorption cross-section. We can safely assume that the three thermal components (narrow, blue wing, and red wing) are the sources of the Compton-scattered photons. The main reflector is likely the primary wind on the opposite side of the emitting source from us during the observation, and therefore sees the opposite plasma motion. (see the discussion in section 4.2). We thus invert the redshift values of the thermal components. This approximation over-simplifies the geometry of the reflector and observer, but still should reasonably describe the scattered emission, as the Compton down-scattering energy is considerably larger than the Doppler shift in the η Carinae spectra.

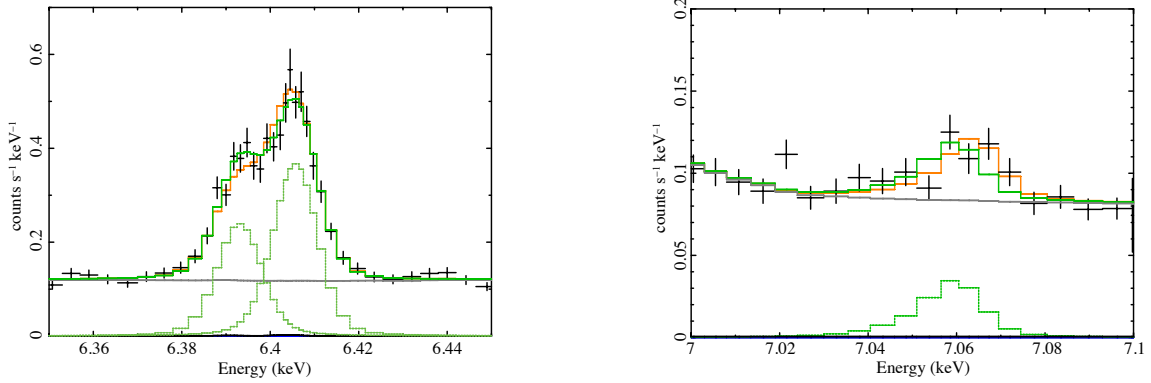


Figure 4. Fluorescent Fe $K\alpha$ (*left*) and $K\beta$ (*right*) line spectra (*black*). The line components are fitted by empirical models in Hölzer et al. (1997), smoothed with the `gsmooth` Gaussian convolution function. For the $K\alpha$ lines, the original model exhibits a non-negligible residual between the $K\alpha_1$ and $K\alpha_2$ lines (*orange*). We thus allow their line normalizations to be independently varied (*green*). For the $K\beta$ lines, we employ a model that ties the redshift and $v_{\sigma 6}$ smoothing parameters to those of the $K\alpha$ model (*green*). However, the best-fit model shows a marginal excess on the blue side, and a model with a free redshift parameter reproduces this excess better (*orange*). We employ the models in green for the entire model fit. The green dotted lines shows the line components, the grey lines represent a thermal model for the continuum, and the blue lines barely above the x-axis represent the non-X-ray background.

For the fluorescent Fe $K\alpha$ and $K\beta$ lines, we refer to the model in Hölzer et al. (1997), which reproduces the line shapes using multiple Lorentzian functions⁶⁷. The observed emission lines are significantly broadened, so we smooth the model using the Gaussian convolution function, `gsmooth` in `Xspec`, fixing the α parameter to 1 with the assumption that the lines are broadened by the same velocity. A fit to the $K\alpha$ line spectrum with an `appec` thermal emission for the continuum moderately reproduces the line profile with a redshift at -3.00×10^{-4} , equivalent to -89.9 km s^{-1} ,⁶⁸ and smoothing sigma at 6 keV (σ_6) at 3.87 eV (193 km s^{-1}). However, the best-fit model shows a small but systematic residual between the $K\alpha_1$ and $K\alpha_2$ lines from the Hölzer et al. (1997) model, which assumes a 2-to-1 theoretical $K\alpha_1 - K\alpha_2$ flux ratio (Figure 4, *left*, orange model). A model that independently varies the $K\alpha_1$ and $K\alpha_2$ line normalizations eliminates this residual (Figure 4, *left*, green model), so we use this model for the entire spectrum fit. For the fluorescent Fe $K\beta$ line, we tied the redshift and `gsmooth` sigma parameters to those of the $K\alpha$ line, but fit the model normalization independently (Figure 4, *right*, green model). We note that the best-fit model leaves a marginal residual on the blue side, which can be reproduced more accurately with an independent redshift value at -9.70×10^{-4} (-291 km s^{-1} ,⁶⁹ Figure 4, *right*, orange model).

The Compton shoulder of the Fe fluorescent $K\alpha$ line is weak, so we tied the redistribution function parameters to those of the Compton scattering of the thermal emission model, and found a good fit. We note that the redistribution function can differ, as the emitting source geometry is distinct: the primary wind for the Fe fluorescence Compton scattering, and the WWC thermal plasma on the WWC shock cone for the thermal Compton scattering.

⁶⁷ The formulae are equivalent to the `feklor` model series in `Xspec`.

⁶⁸ Observed velocity, not converted to the barycentric system.

⁶⁹ 68

3.3. Fitting the XRI240609 Spectrum

We combined all these components into a model and added the best-fit NXB background to the spectral model (see Appendix C). We fit the spectrum between 6.2–7.1 keV with this model using C-statistics (Cash 1979). We estimated the 90% confidence ranges of the fitting parameters using a Markov Chain Monte Carlo (MCMC), Goodman-Weare algorithm built in `Xspec chain`. With 10 walkers, we produced five sets of 10,000 data lengths after burning 200 data lengths. The redshift parameter of the thermal components in XRI240609 was not constrained appropriately, possibly due to an anomalous model behavior near zero. Since the $\text{He}\alpha$ - w line profile mainly constrains the redshift parameter, we evaluate a 90% confidence range for the one-temperature `bapec` model from the 4 band spectrum, after fixing the v_σ parameter to the best-fit value.

The best-fit model reproduces all the spectral profiles very well (Table 2, Figure 5). Three plasma components with a similar brightness, having $kT=4.06$ keV and $Z=0.71$ solar, reproduce both the $\text{He}\alpha$ and $\text{Ly}\alpha$ lines, including the satellite lines. The narrow component has a moderate Doppler broadening of $v_\sigma^{\text{N}} \sim 293$ km s $^{-1}$ but no significant radial velocity. The blue wing component has a maximum blueshift of $v_{\text{max}}^{\text{BW}} \sim -2220$ km s $^{-1}$, while the red wing component has an even higher maximum absolute velocity of $v_{\text{max}}^{\text{RW}} \sim 3107$ km s $^{-1}$. These results are consistent with the picture that the thermal emission originates from collisional equilibrium plasmas streaming from the WWC apex, which moves at a small (< 100 km s $^{-1}$) radial velocity.

A Compton scattering spectrum reflecting 8% of the thermal emission reproduces the excess below the $\text{He}\alpha$ red wing, including the peak at ~ 6.54 keV. The `emcomp` redistribution function (Appendix B.2) is nearly triangular, with the smallest scattering fraction (SSF) at nearly zero. The smallest scattering cut (SSC) value, 0.38, is equivalent to 6.63 keV for the $\text{He}\alpha$ - w line, where the $\text{He}\alpha$ red wing is relatively strong. Since both the smoothing and Compton reflection functions are empirical, the derived SSC value strongly depends on the assumed red wing model, and should be interpreted with caution.

The fluorescent iron lines are significantly blueshifted at ~ -126 km s $^{-1}$ and Doppler broadened by ~ 181 km s $^{-1}$. The $\text{K}\beta$ line accounts for 8.9% of the flux of the $\text{K}\alpha$ line, which is marginally lower than expected from a laboratory measurement (11.3% of the $\text{K}\alpha$ line, Thompson et al. 2009).

3.4. Fitting The Commissioning Phase Observation, XRI231123

XRI231123 shows a very similar *Resolve* spectrum to XRI240609 between 6.2–7.1 keV, except that the count rate is $\sim 68\%$ of that of XRI240609. We therefore used the same spectral model to fit the XRI231123 spectrum. The spectrum lacks sufficient photon statistics to reproduce the Fe fluorescence and Compton shoulder profiles accurately. Meanwhile, the profiles should not vary significantly between the observations with similar shock cone orientations. We, therefore, fixed the Fe fluorescent $\text{K}\alpha$ line ratio and the SSC and SSF values to the best-fit values of XRI240609. Table 2 and Figure 5 display the best-fit parameters.

4. DISCUSSION

4.1. Origin of the Three Thermal Components

The *XRISM Resolve* observations detect three radial velocity components in the Fe $\text{K}\alpha$ thermal plasma emission lines: a narrow component with a Doppler broadening of $v_\sigma^{\text{N}} \sim 300$ km s $^{-1}$, and two wing components with $|v_{\text{max}}| \sim 2100$ – 3100 km s $^{-1}$. *Chandra/HETG* observations, which have previously provided the highest-resolution spectra in this energy band, could measure the average

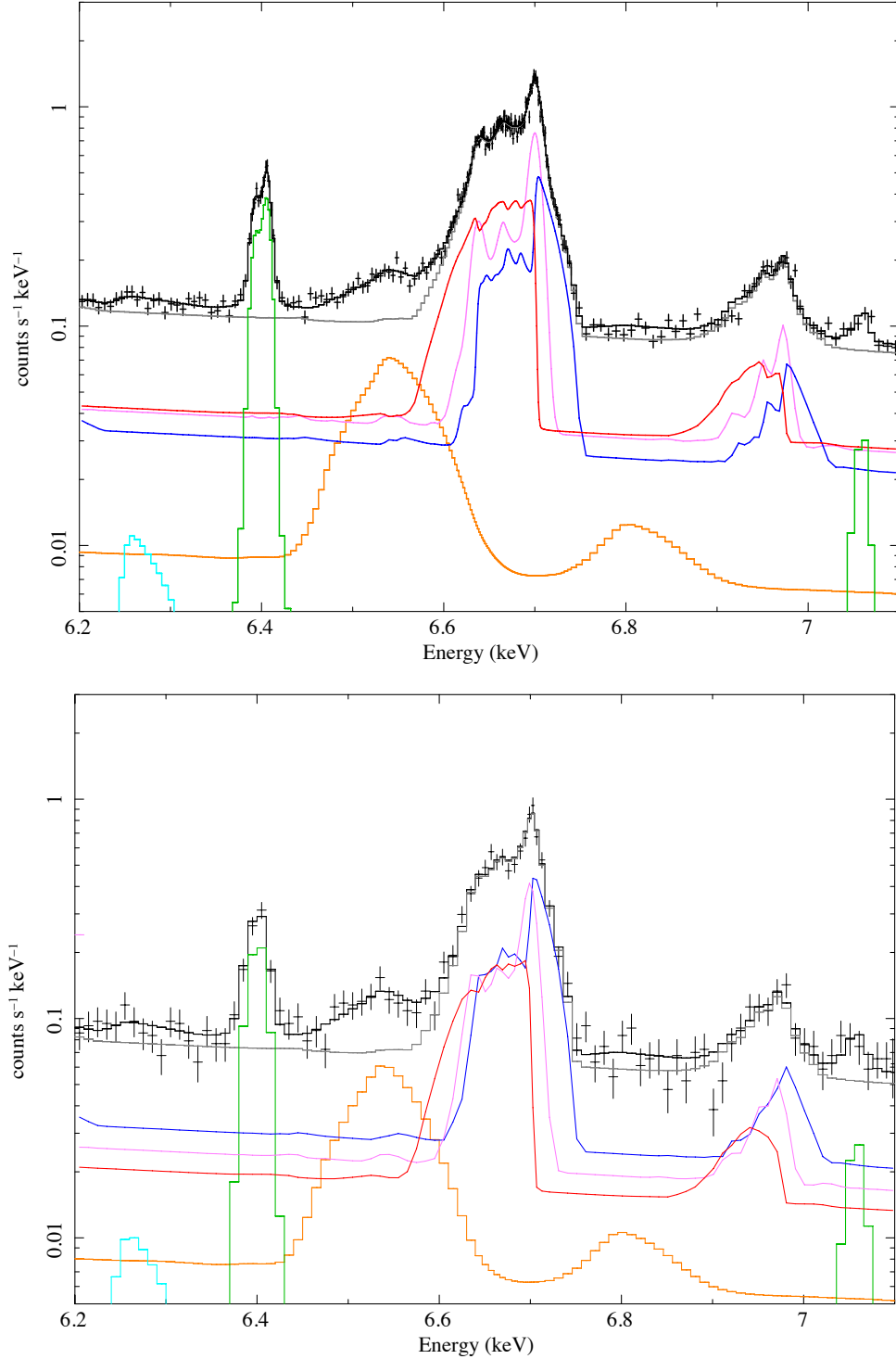


Figure 5. Best-fit model of the Fe $K\alpha$ band spectrum between 6.2–7.1 keV (*top*: XRI240609, *bottom*: XRI231123). The black and grey lines represent the total and the thermal plasma emissions. The blue, purple, and red lines show the blue wing, narrow, and red wing components, and the orange line represents the Compton scattering of these components. The green line shows the Fe fluorescent $K\alpha$ and $K\beta$ lines, and the cyan line shows the Compton scattering of the $K\alpha$ line. The non-X-ray background background, included in the model, is below this plotting scale.

Table 2. Best-Fit Result

Parameters	Unit	XRI231123	XRI240609
Thermal Emission			
kT	(keV)	4.01 (3.79...4.25)	4.060 (4.059...4.062)
Abundance	(solar)	0.68 (0.62...0.79)	0.71 (0.69...0.73)
Redshift [†]	(km/s)	12.8* (−85.6...81.6)	−12.8 ($\pm 27^{\ddagger}$)
Narrow			
Broadening (v_{σ}^N)	(km/s)	332* (269...467)	293 (284...301)
Normalization	(10^{-2})	2.32 (1.64...3.63)	3.69 (3.56...3.85)
Blue Wing			
Maximum Velocity [†]	(km/s)	−2142 (−2387...−2009)	−2220 (−2305...−2136)
Normalization	(10^{-2})	2.90 (2.16...3.18)	2.97 (2.89...3.04)
Red Wing			
Maximum Velocity [†]	(km/s)	2922 (2550...4482)	3107 (2985...3237)
Normalization	(10^{-2})	1.93 (1.12...2.52)	3.85 (3.77...3.94)
Fe Fluorescence			
Broadening ($v_{\sigma 6}$)	(km/s)	319* (271...417)	181 (172...188)
Redshift [†]	(km/s)	−65* (−129...23.4)	−126 (−135...−118)
$K\alpha_1$ flux	(10^{-5} ph/cm ² /s)	2.21 (1.90...2.63)	2.93 (2.79...3.08)
$K\alpha_2$ flux	(10^{-5} ph/cm ² /s)	1.48 (=1.31 $K\alpha_1$)	1.96 (1.91...2.02)
$K\beta$ flux	(10^{-5} ph/cm ² /s)	0.49 (0.31...0.89)	0.44 (0.42...0.45)
Compton Scattering			
CFR		0.103 (0.081...0.136)	0.080 (0.074...0.086)
SSF	(10^{-4})	6.2 (fix)	6.2 (5.5...6.9)
SSC		0.38 (fix)	0.38 (0.36...0.40)
C-Statistic (dof)		2155.23 (1786)	1792.64 (1783)

NOTE— The parentheses show 90% confidence ranges.

[†]These radial velocities are corrected for the solar barycentric system.

[‡]`Xspec/chain` derives an unreasonably small confidence range, perhaps due to an erroneous fitting behavior near zero. This error range is for the redshift parameter of a $1T$ `apex` fit fixing the broadening parameter to the 4-band spectrum, described in Section 3.1.

*These values have additional systematic uncertainties at $\lesssim 1$ eV (~ 45 km s^{−1}).

CFR: Compton Flux Ratio, SSF: Smallest Scattering Fraction, SSC: Smallest Scattering Cut.

radial and broadening velocities of the He α line but lacked the spectral resolution to separate these velocity components. The *XRISM Resolve* spectrum of η Carinae clearly demonstrates the superb energy resolution and efficiency of the *XRISM Resolve* spectrometer in the Fe $K\alpha$ band.

The primary wind with a velocity of 420 km s^{−1} can thermalize gas only up to ~ 0.3 keV (e.g., equation (1) in Luo et al. 1990). The highest temperature can be even lower as the radiative cooling

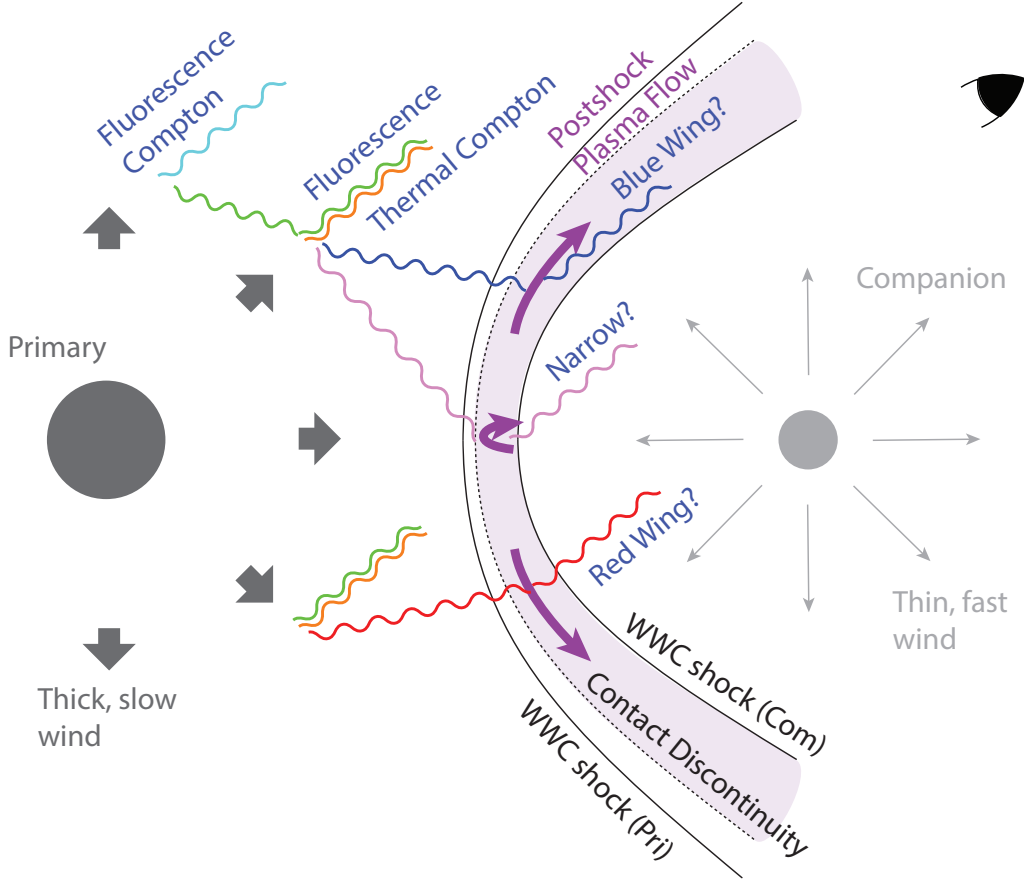


Figure 6. Schematic view of the shock geometry and X-ray emitting locations in the current model. The WWC produces two shocks, one on each side of the wind contact discontinuity. The observed X-ray emission would arise from the post-shock plasma of the companion wind, which is depicted in filled purple. The heated plasma flows down along the WWC contact discontinuity, forming the blue and red wings depending on the flow direction relative to the viewing angle. Some plasma may stand near the stagnation point and emit the narrow component. We observe these X-ray emissions through the cavity produced by the companion wind. Iron atoms in the primary wind absorb the WWC plasma emission above 7.1 keV and re-emit fluorescent lines, while electrons in the wind Compton-scatter the WWC emission. These electrons can also Compton-scatter fluorescing X-rays.

should work efficiently for the post-shock primary wind (see Madura et al. 2013). The observed $kT \sim 4$ keV plasma emission should originate from the post-shock secondary wind with $v \sim 3000$ km s $^{-1}$ and $\dot{M} \sim 10^{-5} M_{\odot}$ yr $^{-1}$ (e.g., Corcoran et al. 1998a; Pittard & Corcoran 2002, see Figure 6).

The wing components have maximum broadening velocities similar to the terminal wind velocity of the companion and far above that of the primary wind. This result again suggests that the $kT \sim 4$ keV plasma originates from the post-shock companion wind. However, the pre-shock wind decelerates with the shock: the post-shock velocity of the head-on collision at the WWC apex should be nearly zero. The post-shock flow downstream adds momentum from oblique collisions and accelerates (see Miyamoto et al. 2024). The high-velocity plasma may have already accelerated at relatively far distances from the WWC apex.

If the downstream plasma flows axis-symmetrically through the contact discontinuity, the velocity profile should have a double-horn structure with peaks near the high and low velocity ends (Henley et al. 2003). However, the observed line profile has a triangular shape with a peak near the center. This may suggest that the observed line profile is not produced solely by a laminar flow of the WWC downstream, but rather by another broadening mechanism, such as turbulence. We note that observed X-ray line profiles from WR 140, a well-known colliding-wind binary system, also exhibit triangular profiles (Miyamoto et al. 2024).

The Fe fluorescence and Compton scattering profiles suggest that the companion star is on our side during these *XRISM* observations (see Section 4.2). In this orientation, the downstream flow should be mainly blueshifted and therefore the blue wing component should be more luminous with a higher absolute maximum velocity than the red wing component. However, the observed red wing has a higher absolute maximum velocity, and a higher flux, at least in XRI240609. This may suggest that the opening angle of the WWC shock cone is near 180° . If so, the companion star has a significantly higher wind velocity and/or mass loss rate than previous estimates, or the primary star has a lower mass loss rate.

The narrow component has a distinct velocity profile from the wing components. It has nearly zero radial velocity at $\sim -12.8 \pm 27$ km s $^{-1}$ and relatively small broadening velocity, $v_\sigma^N \sim 290$ km s $^{-1}$, suggesting that it originates from a slower part of the WWC. *XRISM Resolve* spectra of another WWC binary, WR 140, whose two stars have thin, fast winds ($V_\infty \sim 3000$ km s $^{-1}$), only have broad Fe He α line components of $|v_{\max}| \sim 3000$ km s $^{-1}$ (Hamaguchi et al., private communication). The difference may suggest that the thick, slow primary wind of η Carinae plays a significant role in producing the narrow component.

Although η Carinae’s binary orbital solution is not yet known, the WWC apex should have a low velocity along with the orbital motion during the observations. The optical H β line, which should trace the primary wind, has radial velocities of 0–10 km s $^{-1}$ (Strawn et al. 2023). This implies that the WWC apex radial velocity is within ± 10 km s $^{-1}$, assuming the presumed stellar mass ratio of ~ 2 – 3 and wind momentum ratio of 0.12–0.42. The redshift of the narrow component is consistent with the WWC apex’s radial motion. This narrow component may arise from the shock-stagnation point of the companion wind, where the relative flow velocity is nearly zero. However, the stagnation point is theoretically a point, and it is not clear if such a low velocity region can, in reality, be large enough to produce emission comparable to each high-velocity wing component. Alternatively, a part of the post-shock companion wind near the apex may penetrate the primary wind and interact with the relatively cold primary wind. This hypothesis may explain why the broadening velocity is close to the primary wind velocity and the WR 140 spectra do not show a similar narrow component.

4.2. Geometry of the WWC Shock

The observed fluorescent Fe K α lines are significantly blueshifted compared to those from neutral Fe at the rest frame. Although the line energies change with ionization, most iron atoms in the cold primary wind do not exceed the charge state Fe $^{3+}$ (e.g., Madura et al. 2013), and the line centroid energies remain unchanged within this ionization range (Yamaguchi et al. 2014). The observed blueshift reflects the radial velocity of the fluorescing matter rather than ionization.

About 90% (1.62σ) of the fluorescent photons in XRI240609 are within the primary wind’s radial velocity range between -420 km s $^{-1}$ and $+168$ km s $^{-1}$. The lower end, -420 km s $^{-1}$, is the blueshifted terminal velocity of a stream of the primary wind flowing toward us. The higher range between $+168$

and $+420 \text{ km s}^{-1}$ is absent, plausibly due to a thick optical depth to the far side of the primary wind. This result strongly suggests that the fluorescent Fe lines mainly originate in the primary wind viewed from a side of the companion. This geometry may also explain the apparent $K\alpha_2/K\alpha_1$ flux ratio anomaly: a fluorescing line from an optically thick, spherical wind at an oblique angle to the irradiating source produces an asymmetric line profile with a red tail.

Compton scattering occurs in any medium with electrons, free or bound, and should happen on the paths that produce Fe K fluorescence as well. The best-fit `emcomp` distribution function has a triangular shape with more backscattering photons, again indicating that the majority of the scattering medium lies behind the emitting source, i.e., the WWC plasma, as seen from us. The best-fit result shows little scattering below $\text{SSC} = 0.38$, corresponding to a scattering angle of $\approx 76^\circ$, suggesting little scattering matter along the line of sight and the wind half-opening angle at $\approx 76^\circ$ or larger. It is larger than the half-opening angle of the WWC shock cone of $55\text{--}75^\circ$ expected from the wind velocities and mass loss rates (e.g., Madura et al. 2013), but largely consistent considering a hidden uncertainty of the SSC measurement.

The best-fit Compton Flux Ratio (CFR) suggests that $\sim 8\%$ of the source emission is reflected with Compton scattering. Since 80% of the photons on the scattering paths, assuming the elemental abundance discussed in Section 4.3, suffer photoelectric absorption, the primary wind as scattering matter should subtend $\sim 1.6\pi$ steradians from the emitting source, which is equivalent to the companion wind's half-opening angle at $\sim 110^\circ$, if it is optically thick. Since some scattering paths away from the primary star would be optically thin, this provides an upper limit of the wind opening angle, consistent with the above constraint.

All these results indicate that the primary wind is on the opposite side of the WWC apex from us, i.e., the companion star is on our side, during the observations. This orientation is consistent with the several orbital models constrained from optical or X-ray emission line profiles (e.g., Strawn et al. 2023; Russell et al. 2016; Madura et al. 2013; Henley et al. 2008) but not the models based on the assumption that the absorption increase near periastron originates from mass accretion onto the companion star (e.g., Kashi et al. 2021; Kashi & Soker 2009).

4.3. Elemental Abundance of the Primary Wind

Intensities of the Compton-scattered emission and the Fe fluorescent line are proportional to the number of electrons and Fe atoms, respectively, so their flux ratio constrains the elemental abundance of the primary wind. To minimize the effects of absorption and the uncertainty in the `emcomp` distribution function, we evaluate the Compton-scattered emission at 6.4 keV, the Fe fluorescent line energy and use the line equivalent width (EW), defined as the intensity ratio of the Fe $K\alpha$ fluorescence line (the $K\alpha_1 + K\alpha_2$ flux in Table 2) to the Compton scattering continuum (the orange line in each panel of Figure 5) at 6.4 keV.

This measurement provides a robust estimate of the number of electrons per Fe atom, which is $\sim (N(\text{H}) + 2N(\text{He}))/N(\text{Fe})$ as H and He are the dominant electron carriers. H and He are key elements for understanding stellar evolutionary stages, but measuring their abundances using UV or optical emission lines is challenging due to inherent uncertainties in their ionization and chemical states. This X-ray measurement is largely unaffected by the ionization or chemical state of the primary wind, though it cannot count each element separately.

The EW s of the best-fit models are ~ 947 (73) eV for XRI240609 and 834 (155) eV for XRI231123, where the values in parentheses indicate the 90% confidence ranges. We evaluate the expected EW s

for a 1 solar (**asp1**) elemental abundance absorber irradiated by $kT=4$ keV plasma emission. First, we calculate these values numerically for an optically-thin absorber, using the Thomson scattering cross-section, which averages out the angular dependence of Compton scattering, for simplicity. At each photon energy E , the Compton scattered flux is $\text{SRC}(E) \times N_e \times \sigma_{\text{TH}}$, and the flux absorbed by Fe atoms in the wind is $\text{SRC}(E) \times N_{\text{Fe}} \times \sigma_{\text{Fe}}^{\text{abs}}(E)$, with $\text{SRC}(E)$ being the incident flux at energy E , N_e the column density of electrons, N_{Fe} , the Fe column density, and σ_{TH} and $\sigma_{\text{Fe}}^{\text{abs}}(E)$ the Thomson scattering and Fe absorption cross sections, respectively. For the EW of the Fe $K\alpha$ fluorescence line, we integrate the flux absorbed by Fe atoms between 7.11 keV and 28 keV⁷⁰, and multiply this by the Fe fluorescence yield (35.1%) and the flux ratio of the $K\alpha$ lines (89.8%, Thompson et al. 2009). Dividing the Fe $K\alpha$ integrated line flux by the Thomson scattered continuum at 6.4 keV, we obtain an EW of 582 eV. We also consider the more realistic case of an optically-thick absorber using the Monte Carlo radiative transfer code, SKIRT (Vander Meulen et al. 2023, 2024), assuming a point-like, 4 keV thermal source seen through a flat, optically-thick slab (similar to the geometry in section 4.1.2 of Vander Meulen et al. 2023). The simulations indicate an EW of 584 eV when electrons are bound to atoms, and at 559 eV when electrons are unbound to atoms. Both the numerical and simulation results suggest that the EW does not depend significantly on the optical thickness or the ionization of the absorber. The observed EW is about 60% higher than any of the calculated values assuming the **asp1** solar abundance medium (Asplund et al. 2009).

Contamination of the primary wind by CNO nuclear fusion products would primarily cause the electron depletion. The CNO cycle produces one He atom from four H atoms, diminishing the number of electrons by 2. CNO processing also increases N and decreases C and O (Davidson et al. 1982; Leutenegger et al. 2003). However, since CNO act as catalysts, the total number of CNO nuclei remains constant, and therefore the total number of electrons in the nitrogen-enhanced gas changes by less than 4%. We simulate how the H and He abundances change from a solar abundance gas due to nuclear fusion, and calculate an EW at each set of abundances, assuming no C or O atoms, and 12.2 solar for N, and abundances of other elements at 1 solar. Then, the abundances of H at 0.16 solar and He at 3.47 solar, $N(\text{H})/N(\text{He})=0.54$, or the H mass ratio at ~ 0.12 , provide an EW at ~ 948 eV, nearest to the observed value.

Such a low H abundance on the stellar surface is predicted in the late *LBV* or nitrogen-rich Wolf-Rayet (WN) phase according to a stellar evolution model for a non-rotating $60 M_{\odot}$ star (Groh et al. 2014). Eta Carinae is expected to have a significantly larger initial mass of $\sim 150 M_{\odot}$ (Hillier et al. 2001), and therefore the result may not be directly applicable. Still, the result may suggest that He-burning in the stellar core might already have started. In the meantime, the derived $N(\text{H})/N(\text{He})$ ratio is significantly smaller than the assumption in Hillier et al. (2001) for constraining the mass of η Carinae. If this value is correct, the primary star's mass loss rate would be higher by a factor of ~ 4.7 and that the minimum total mass of the two stars would be smaller to $\sim 87 M_{\odot}$ (see Sections 9.1 and 12 of Hillier et al. 2001).

An enhanced Fe abundance also results in a high EW . While most abundance tables have similar Fe abundances⁷¹ to the **asp1** table we adopt, the **anгр** abundance table (Anders & Grevesse 1989) has a $\sim 48\%$ higher Fe abundance than the **asp1** table. This Fe abundance yields a calculated EW of 806 eV with 1 solar H and He abundances, which is still lower than the observed value. Note that

⁷⁰ Note that more than 80% of the fluorescent emission originate from incident photons between 7.11–10 keV

⁷¹ see <https://heasarc.gsfc.nasa.gov/xanadu/xspec/manual/node116.html>

the Fe and Ni emission lines from hot plasmas in the *Resolve* spectra are in better agreement with a model using the `asp1` table, while the `anгр` abundance table significantly overpredicts the Fe He α line strength relative to the Ni He α line.

5. CONCLUSIONS

XRISM observed the supermassive stellar binary system, η Carinae, which drives the most vigorous wind-wind collision X-ray activity within 3 kpc, in 2023 November ($\phi_X = 0.68$) and 2024 June ($\phi_X = 0.78$). The *Resolve* X-ray micro-calorimeter observations provided unprecedented energy resolution spectra of the binary system between 1.7–12 keV, which clearly separate emission lines from major elements, Ni, Fe, Ca, Ar, S, and Si as well as detect weak lines from rare elements such as Mn and Cr. In particular, the spectra exhibit the detailed structure in the Fe K α band between 6.2–7.1 keV for the first time, revealing multiple velocity components in the Fe He α and Ly α thermal emission lines, Doppler motions of the fluorescent Fe K α and K β lines, and the presence of their Compton-scattered emissions — arguably the first clear detection of the Compton shoulder of thermal X-ray emission lines from celestial sources.

The Fe He α and Ly α thermal emission lines are significantly broadened, blending individual emission lines, including He α satellite lines. The broadening line profile requires three velocity components, narrow, blue wing and red wing, of $kT \sim 4$ keV collisional equilibrium plasmas, but it does not require exotic states such as non-equilibrium plasmas. These plasmas have similar characteristics to those observed in earlier η Carinae at this orbital phase. The two wing components can be reproduced with asymmetric broadening shapes with maximum radial velocities at ~ 2100 – 3200 km s $^{-1}$. These velocities are close to the terminal velocity of the companion wind, suggesting that these components originate from the post-shock companion wind flowing through the contact discontinuity. However, the observed triangular velocity distribution does not match the double-horn profile expected from a laminar flow through the shock cone: it may require an additional broadening mechanism, such as turbulence within the flow. In contrast, the narrow component has a negligible radial velocity with small broadening at $v_\sigma^N \sim 293$ km s $^{-1}$. These velocity profiles suggest that the plasma is trapped at the stagnation point at the WWC apex and/or penetrated into the primary wind.

The XRI240609 spectrum clearly separates the Fe fluorescent K α_1 and K α_2 lines at ~ 6.4 keV and detects the Fe fluorescent K β lines. These lines exhibit a significant blueshift by ~ -126 km s $^{-1}$ and a broadening of ~ 181 km s $^{-1}$ with a marginal asymmetrical broadening structure. The XRI231123 spectrum also shows a similar result with limited statistics. Both spectra also exhibit He α Compton shoulder emission between 6.45–6.60 keV clearly, as well as Compton shoulder profiles associated with the Ly α and fluorescent Fe K α lines marginally. The emission profile suggests strong backscattering emission and little forward scattering emission. Both the Fe fluorescent line dynamics and the Compton scattering profile indicate that the absorbing and scattering medium is the primary wind on the opposite side of the WWC plasma from us, i.e., the companion star is on our side, during the observations.

The flux ratio of the Fe fluorescent line over the Compton scattering is significantly larger than that expected from a solar abundance absorber or scatter, indicating that the primary wind is heavily depleted in electrons. This phenomenon can be explained by the contamination of the primary wind with nuclear fusion products from the CNO cycle, which converts 4 H atoms into 1 He atom. Assuming that the Fe abundance does not change with stellar evolution, the observed ratio requires a

very low H abundance of ~ 0.16 solar, which can be realized in a late *LBV* phase in a stellar evolution model.

These unprecedented details of the *XRISM/Resolve* Fe K-band spectra provide valuable insights into the conditions of both hot and cold gases, but also introduce further mysteries. Addressing those questions requires more in-depth analyses of the data, including emission lines beyond the 6.2–7.1 keV range. This includes examining Si, S, Ar and Ca lines between 2–5 keV, as well as Ni and Fe He β , γ lines beyond 7.1 keV, and utilizing more advanced modelings. Additionally, some perplexing issues, such as the “narrow” component, will necessitate further *XRISM* observations of η Carinae during different binary orbital phases and other massive WWC stellar binary systems.

ACKNOWLEDGMENTS

We appreciate fruitful discussions with Drs. Augusto Damineli, Theodor R. Gull, D. John Hillier, Jonathan Mackey, Anthony F.J., Moffat, Yaël Nazé, Julian M. Pittard, Noel Richardson, Christopher Russell, and Gerd Weigelt. The material is based upon work supported by NASA under award numbers 80GSFC21M0002, 80GSFC24M0006, 80NSSC18K1684, 80NSSC18K0988, 80NSSC20K0733, 80NSSC20K0737, 80NSSC20K0883, 80NSSC22K1922, 80NSSC23K1656, 80NSSC24K0678, 80NSSC24K1148, 80NSSC24K1774, 80NSSC25K7064, and 80NSSC25K7536, and contract NAS8-0360. This work is supported by JSPS KAKENHI grant numbers JP19K14762, JP19K21884, JP20H00157, JP20H01946, JP20H01947, JP20H05857, JP20K04009, JP20K14491, JP20KK0071, JP21H01095, JP21H04493, JP21K03615, JP21K13958, JP21K13963, JP22H00158, JP23H00121, JP23H00151, JP23H01211, JP23K03454, JP23K03459, JP23H04899, JP23K13154, JP23K20239, JP23K20850, JP23K22548, JP23KJ1807, JP24H00253, JP24K00638, JP24K00672, JP24K00677, JP24K17093, JP24K17104, JP24K17105, JP25H00672, and JP25K01026. This work is supported by Lawrence Livermore National Laboratory under Contract DE-AC52-07NA27344, STFC through grant ST/T000244/1, Canadian Space Agency grant 18XARMSTMA, the Alfred P. Sloan Foundation through the Sloan Research Fellowship, the JSPS Core-to-Core Program, JPJSCCA20220002, the RIKEN Pioneering Project Evolution of Matter in the Universe (r-EMU), the RIKEN SPDR Program, Rikkyo University Special Fund for Research (Rikkyo SFR), the Kagoshima University postdoctoral research program (KU-DREAM), the Strategic Research Center of Saitama University, Program for Forming Japan’s Peak Research Universities (J-PEAKS), and the Organization for the Promotion of Gender Equality at Nara Women’s University.

Facilities: XRISM(Resolve, Xtend)

Software: HEASoFT (Nasa High Energy Astrophysics Science Archive Research Center (Heasarc) 2014), xspec (Arnaud 1996), scipy (Virtanen et al. 2020), astropy (Astropy Collaboration et al. 2013), AtomDB ver. 3.1.2 (Foster et al. 2012)

APPENDIX

A. GAIN RECALIBRATION OF THE XRI231123 DATA

This observation was performed during the commissioning phase of the *XRISM* observatory when many of the methods used for calibrating the instruments were developed. The *Resolve* instrument,

in particular, requires careful calibration of the time-dependent energy scale during each observation. The time-dependent energy scale is dependent on extrinsic factors including the heat sink temperature for the 50 mK focal plane, the amount of bolometric loading, and the temperature of the instrument electronics which affects the gain and bias current for the detector system. The original plan was to use the on-board modulated X-ray sources (MXS) to periodically perform this calibration during each observation (Sawada et al. 2024). Unfortunately, the instrument gate valve did not open as planned, and the MXS could only illuminate about half of the array. Thus the current strategy is to use ^{55}Fe radioactive X-ray sources mounted on the instrument’s filter wheel (FW) to periodically provide fiducial measurements of the gain, and thus the energy scale, of the instrument. The periodic measurements of the 5.9 keV Mn $K\alpha$ from the FW is used linear interpolate between fiducial measurements and to synthesize the non-linear gain scale for each X-ray event (Porter et al. 2016, 2024). Unfortunately, this observation was performed before this process was established.

For this observation, the closest fiducial measurement was about two days before the observation, and there were no fiducial measurements during the observation. Instead, we used the last fiducial measurement for each pixel and extrapolated the gain of each pixel forward using a calibration pixel located outside of the field of view of the instrument. The calibration pixel is part of the focal plane array but located off to the side of the instrument field of view. It is continuously illuminated by a heavily collimated dedicated ^{55}Fe X-ray source. The reason that the calibration pixel is not the sole gain calibrator for the entire array is due to differential bolometric loading between pixels in the focal plane and time-dependent changes in the detector bias that can cause the gain of the pixels to diverge over long periods of time. However, during short intervals, such as the two days between the last fiducial measurement and this observation, the divergence is small, likely better than 1 eV at 6 keV. Figure 7 shows the time dependent energy scale for this observation for each pixel as synthesized from the last known fiducial measurement projected forward by the calibration pixel. A gain history fits file meeting the requirements of the *Resolve* energy assignment `rs1pha2pi` tool was constructed using the time- and pixel-dependent effective temperature. The archived data was then reprocessed using the `xpipeline` reprocessing script with the `calmethod` parameter set to ‘Cal-pix’ and the `userghf` parameter set to the custom gain history file. In this mode, the script will construct a gain history file in the usual way (which is why the calibration pixel method was chosen), but will apply the file designated by the `userghf` setting.

B. XSPEC LOCAL MODELS

We develop `Xspec` convolution models that empirically reproduce asymmetrically broadened or Compton down-scattered spectra⁷². These models utilize the `calcManyLines` generic code in `Xspec`, used in the `gsmooth` function and other smoothing functions.

B.1. *Htsmooth*

This model, `htsmooth` (Half-Triangle SMOOTH, Figure 8 *left*), redistributes the flux within each spectral bin (Ebin) to a half-triangular distribution. The model includes a single parameter, `MaxVel`, in the unit of km s^{-1} , which represents the maximum radial velocity in the absolute value at the end of the half-triangle. A negative `MaxVel` value indicates a blueshift, while a positive value indicates a redshift, extending the triangle into the higher or lower energy range, respectively.

⁷² These codes are available on https://github.com/HEASARC/xspec_localmodels/tree/master/redistmodels

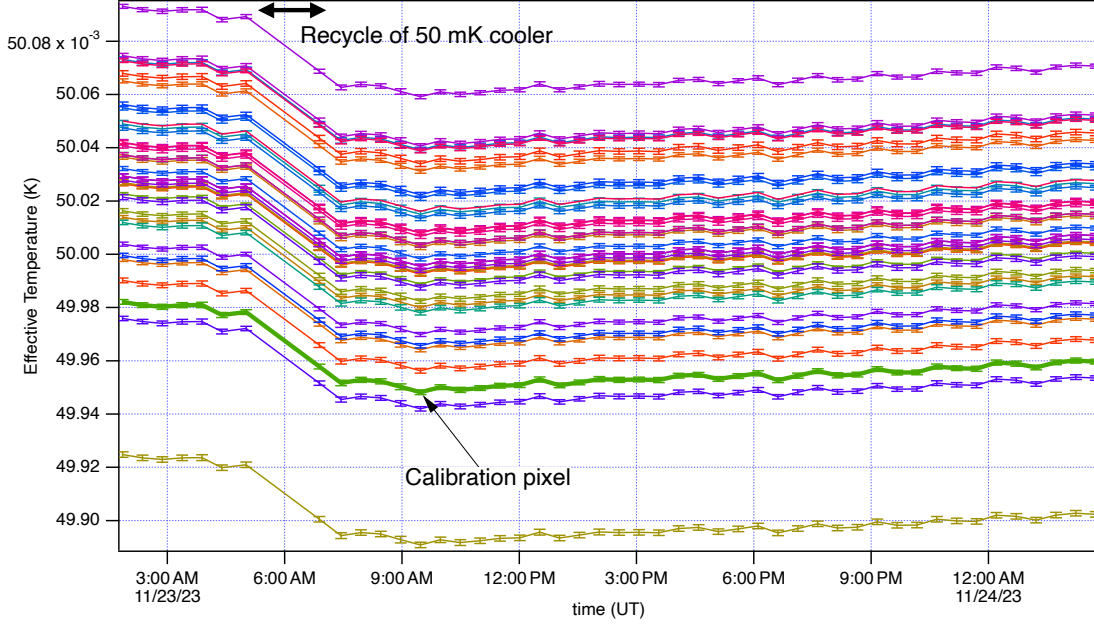


Figure 7. The time dependent energy scale (detector gain) vs time at 5.9 keV synthesized from the last known fiducial measurement and a continuous measurement using the calibration pixel (heavy green). The detector gain is parameterized as "effective" pixel temperature (Porter et al. 2016) and each pixel is a different color.

B.2. *Emcomp*

This model, *emcomp* (EMpirical COMPTon, Figure 8 right), redistributes the flux within each spectral bin (E_{bin}) to a trapezoidal distribution, defined down to the 180° Compton backscattering energy (E_{BS}) using the Smallest Scattering Fraction (SSF), Largest Scattering Fraction (LSF), and Smallest Scattering Cut (SSC). The 180° -degree Compton backscattering energy E_{BS} is:

$$E_{\text{BS}} = \frac{E_{\text{bin}}}{1 + 2(E_{\text{bin}}/511 \text{ keV})} \quad (\text{B1})$$

The Compton Flux Ratio (CFR) parameter is the ratio of the Compton-scattering flux to the source flux. After conducting preliminary trials, the LSF parameter is fixed at 1 to prevent any issues with degeneracy. This model is empirical and does not account for the angular dependence of the Compton scattering cross-section. It is important to note that in a cold medium, photoelectric absorption occurs with Compton scattering. The Compton scattering cross-section is relatively constant within the *XRISM* X-ray energy range, while the absorption cross-section is smaller at a higher energy. Consequently, the optical depth changes, and the total Compton-scattering flux changes with energy. This model does not account for this effect and, therefore, is not suitable for wide-band fitting.

C. BEST-FIT NON-X-RAY BACKGROUND MODEL

The following table shows the best-fit parameters of the NXB v1 model (*rsl_nxb_model.v1.mo*) to the NXB spectra, which are extracted from the provisional NXB database collected between Dec. 25, 2023 and May 24, 2024.

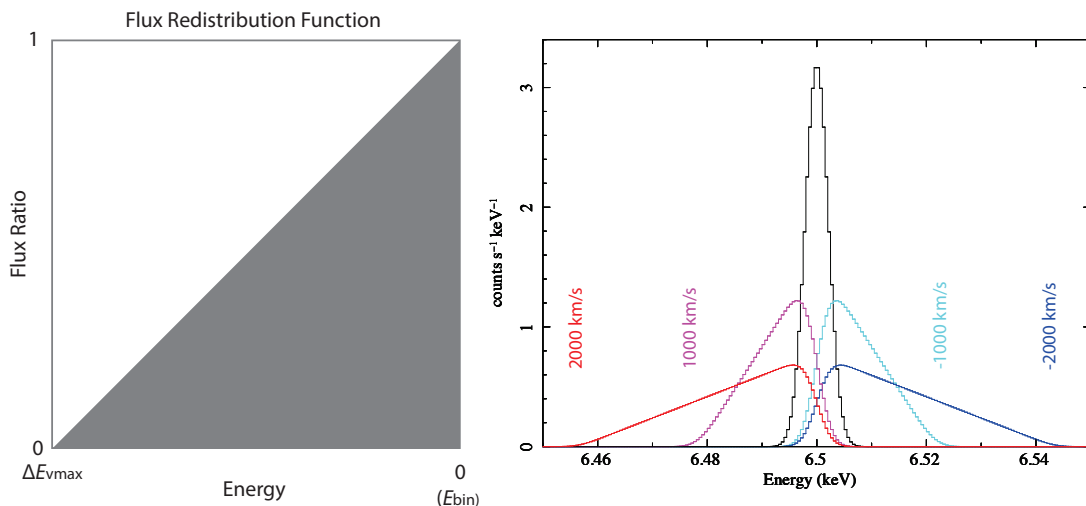


Figure 8. *Left:* Redistribution function of the `htsmooth` model. The corresponding energy of the free model parameter, v_{\max} , is indicated on the figure. *Right:* The function applied to a Gaussian line at 6.5 keV (*black*). The MaxVel parameter for each model is displayed in its designated color. All models are convolved with a response function for *Resolve* Hp events.

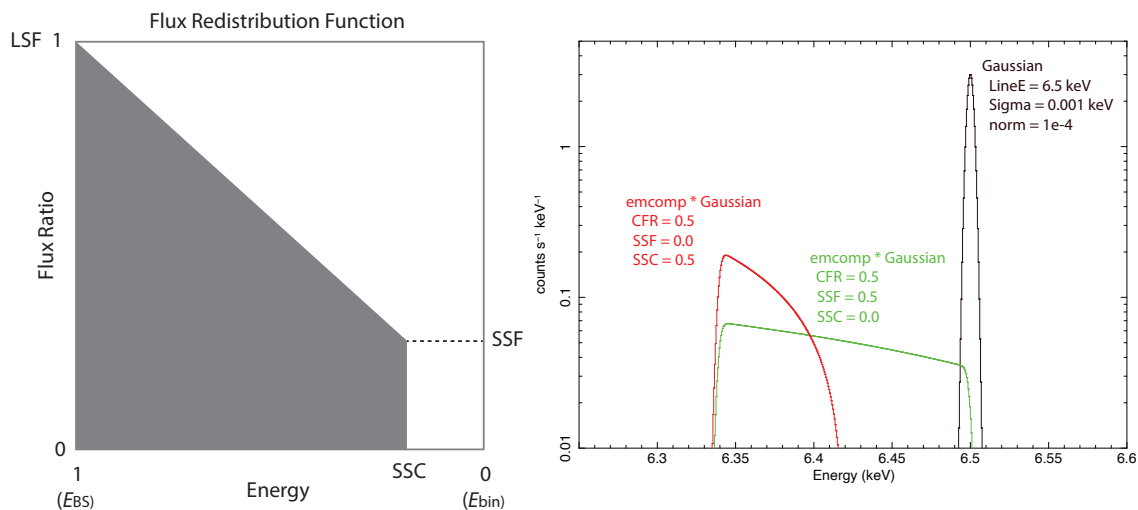


Figure 9. *Left:* Redistribution function of the `emcomp` model. The free model parameters SSC, SSF, and LSF are indicated on the figure. *Right:* The function applied to a Gaussian function at 6.5 keV (*black*). All models are convolved with a response function for *Resolve* Hp events.

Table 3. NXB Model

Parameter	XRI231123	XRI240609
1	0.990114	0.965222
3	8.21591E-04	8.21591E-04
7	3.84967E-05	4.16577E-05
14	2.86589E-05	2.11130E-05
20	4.82967E-05	3.72466E-05
23	1.11295E-05	1.24417E-05
29	8.19269E-06	1.22293E-05
35	3.97141E-05	4.50395E-05
41	1.75562E-05	2.11823E-05
47	2.22964E-05	1.43713E-05
50	1.58155E-04	1.70030E-04
53	1.40780E-04	1.42236E-04
56	4.16170E-05	4.85166E-05

NOTE— Par: the sequential parameter numbers of the NXB v1 model, which appear in Xspec outputs.

REFERENCES

- Anders, E., & Grevesse, N. 1989, *GeoCoA*, 53, 197
- Arnaud, K. A. 1996, in *Astronomical Society of the Pacific Conference Series*, Vol. 101, *Astronomical Data Analysis Software and Systems V*, ed. G. H. Jacoby & J. Barnes, 17
- Asplund, M., Grevesse, N., Sauval, A. J., & Scott, P. 2009, *ARA&A*, 47, 481
- Astropy Collaboration, Robitaille, T. P., Tollerud, E. J., Greenfield, P., Droettboom, M., Bray, E., Aldcroft, T., Davis, M., Ginsburg, A., Price-Whelan, A. M., Kerzendorf, W. E., Conley, A., Crighton, N., Barbary, K., Muna, D., Ferguson, H., Grollier, F., Parikh, M. M., Nair, P. H., Unther, H. M., Deil, C., Woillez, J., Conseil, S., Kramer, R., Turner, J. E. H., Singer, L., Fox, R., Weaver, B. A., Zabalza, V., Edwards, Z. I., Azalee Bostroem, K., Burke, D. J., Casey, A. R., Crawford, S. M., Dencheva, N., Ely, J., Jenness, T., Labrie, K., Lim, P. L., Pierfederici, F., Pontzen, A., Ptak, A., Retsdal, B., Servillat, M., & Streicher, O. 2013, *A&A*, 558, A33
- Behar, E., Nordon, R., & Soker, N. 2007, *ApJL*, 666, L97
- Cash, W. 1979, *ApJ*, 228, 939
- Corcoran, M. F., Fredericks, A. C., Petre, R., Swank, J. H., & Drake, S. A. 2000, *ApJ*, 545, 420
- Corcoran, M. F., Ishibashi, K., Davidson, K., Swank, J. H., Petre, R., & Schmitt, J. H. M. M. 1997, *Nature*, 390, 587
- Corcoran, M. F., Liburd, J., Morris, D., Russell, C. M. P., Hamaguchi, K., Gull, T. R., Madura, T. I., Teodoro, M., Moffat, A. F. J., Richardson, N. D., Hillier, D. J., Damineli, A., & Groh, J. H. 2017, *ApJ*, 838, 45
- Corcoran, M. F., Petre, R., Swank, J. H., Drake, S. A., Koyama, K., Tsuboi, Y., Viotti, R., Damineli, A., Davidson, K., Ishibashi, K., White, S., & Currie, D. 1998a, *ApJ*, 494, 381
- . 1998b, *ApJ*, 494, 381
- Corcoran, M. F., Rawley, G. L., Swank, J. H., & Petre, R. 1995, *ApJL*, 445, L121
- Corcoran, M. F., Swank, J. H., Petre, R., Ishibashi, K., Davidson, K., Townsley, L., Smith, R., White, S., Viotti, R., & Damineli, A. 2001, *ApJ*, 562, 1031
- Cox, P., Mezger, P. G., Sievers, A., Najarro, F., Bronfman, L., Kreysa, E., & Haslam, G. 1995, *A&A*, 297, 168
- Damineli, A. 1996, *ApJL*, 460, L49+
- Damineli, A., Hillier, D. J., Corcoran, M. F., Stahl, O., Levenhagen, R. S., Leister, N. V., Groh, J. H., Teodoro, M., Albacete Colombo, J. F., Gonzalez, F., Arias, J., Levato, H., Grosso, M., Morrell, N., Gamen, R., Wallerstein, G., & Niemela, V. 2008, *MNRAS*, 384, 1649
- Davidson, K., Ebbets, D., Weigelt, G., Humphreys, R. M., Hajian, A. R., Walborn, N. R., & Rosa, M. 1995, *AJ*, 109, 1784
- Davidson, K., Walborn, N. R., & Gull, T. R. 1982, *ApJL*, 254, L47
- Espinoza-Galeas, D., Corcoran, M. F., Hamaguchi, K., Russell, C. M. P., Gull, T. R., Moffat, A. F. J., Richardson, N. D., Weigelt, G., Hillier, D. J., Damineli, A., Stevens, I. R., Madura, T., Gendreau, K., Arzoumanian, Z., & Navarete, F. 2022, *ApJ*, 933, 136
- Foster, A. R., Ji, L., Smith, R. K., & Brickhouse, N. S. 2012, *ApJ*, 756, 128
- Groh, J. H., Hillier, D. J., Madura, T. I., & Weigelt, G. 2012, *MNRAS*, 423, 1623
- Groh, J. H., Meynet, G., Ekström, S., & Georgy, C. 2014, *A&A*, 564, A30
- Hamaguchi, K., Corcoran, M. F., Gull, T., Ishibashi, K., Pittard, J. M., Hillier, D. J., Damineli, A., Davidson, K., Nielsen, K. E., & Kober, G. V. 2007, *ApJ*, 663, 522
- Hamaguchi, K., Corcoran, M. F., Gull, T. R., Takahashi, H., Grefenstette, B. W., Yuasa, T., Stuhlinger, M., Russell, C. M. P., Moffat, A. F. J., Sharma, N., Madura, T. I., Richardson, N. D., Groh, J., Pittard, J. M., & Owocki, S. 2016, *ApJ*, 817, 23
- Hamaguchi, K., Corcoran, M. F., Pittard, J. M., Sharma, N., Takahashi, H., Russell, C. M. P., Grefenstette, B. W., Wik, D. R., Gull, T. R., Richardson, N. D., Madura, T. I., & Moffat, A. F. J. 2018, *Nature Astronomy*, 2, 731
- Hamaguchi, K., Corcoran, M. F., Russell, C. M. P., Pollock, A. M. T., Gull, T. R., Teodoro, M., Madura, T. I., Damineli, A., & Pittard, J. M. 2014a, *ApJ*, 784, 125

- Hamaguchi, K., Corcoran, M. F., Takahashi, H., Yuasa, T., Ishida, M., Gull, T. R., Pittard, J. M., Russell, C. M. P., & Madura, T. I. 2014b, *ApJ*, 795, 119
- Hayashi, T., Boissay-Malaquin, R., Tamura, K., Okajima, T., Eckart, M. E., Leutenegger, M. A., Yaqoob, T., Loewenstein, M., Kelley, R. L., Porter, F. S., Kilbourne, C. A., Chiao, M. P., Sneiderman, G. A., Cumbee, R. S., Ishisaki, Y., Fujimoto, R., Tsujimoto, M., Sawada, M., Sato, T., Maeda, Y., Ishida, M., Corrales, L., Miller, E., Tumer, A., Takahashi, H., Brenneman, L., Kanemaru, Y., Mizumoto, M., Markevitch, M., & Guainazzi, M. 2024, in *Society of Photo-Optical Instrumentation Engineers (SPIE) Conference Series*, Vol. 13093, *Space Telescopes and Instrumentation 2024: Ultraviolet to Gamma Ray*, ed. J.-W. A. den Herder, S. Nikzad, & K. Nakazawa, 130931L
- Henley, D. B., Corcoran, M. F., Pittard, J. M., Stevens, I. R., Hamaguchi, K., & Gull, T. R. 2008, *ApJ*, 680, 705
- Henley, D. B., Stevens, I. R., & Pittard, J. M. 2003, *MNRAS*, 346, 773
- Hillier, D. J., Davidson, K., Ishibashi, K., & Gull, T. 2001, *ApJ*, 553, 837
- Hölzer, G., Fritsch, M., Deutsch, M., Härtwig, J., & Förster, E. 1997, *PhRvA*, 56, 4554
- Ishibashi, K., Corcoran, M. F., Davidson, K., Swank, J. H., Petre, R., Drake, S. A., Damineli, A., & White, S. 1999, *ApJ*, 524, 983
- Kashi, A., Principe, D. A., Soker, N., & Kastner, J. H. 2021, *ApJ*, 914, 47
- Kashi, A., & Soker, N. 2009, *MNRAS*, 397, 1426
- Kelley, R. 2024, in *AAS/High Energy Astrophysics Division*, Vol. 21, *AAS High Energy Astrophysics Division Meeting #21*, 303.01
- Leutenegger, M. A., Kahn, S. M., & Ramsay, G. 2003, *ApJ*, 585, 1015
- Leyder, J.-C., Walter, R., & Rauw, G. 2008, *A&A*, 477, L29
- . 2010, *A&A*, 524, A59
- Luo, D., McCray, R., & Mac Low, M.-M. 1990, *ApJ*, 362, 267
- Madura, T. I., Gull, T. R., Okazaki, A. T., Russell, C. M. P., Owocki, S. P., Groh, J. H., Corcoran, M. F., Hamaguchi, K., & Teodoro, M. 2013, *MNRAS*, 436, 3820
- Mehner, A., Davidson, K., Ferland, G. J., & Humphreys, R. M. 2010, *ApJ*, 710, 729
- Miyamoto, A., Sugawara, Y., Maeda, Y., Ishida, M., Hamaguchi, K., Corcoran, M., Russell, C. M. P., & Moffat, A. F. J. 2024, *MNRAS*, 527, 7121
- Mori, K., Tomida, H., Nakajima, H., Okajima, T., Noda, H., Uchida, H., Suzuki, H., Kobayashi, S. B., Yoneyama, T., Hagino, K., Nobukawa, K., Tanaka, T., Murakami, H., Uchiyama, H., Nobukawa, M., Matsumoto, H., Tsuru, T., Yamauchi, M., Hatsukade, I., Odaka, H., Kohmura, T., Yamaoka, K., Ishida, M., Maeda, Y., Hayashi, T., Tamura, K., Boissay-Malaquin, R., Sato, T., Yoshida, T., Kanemaru, Y., Hiraga, J., Dotani, T., Ozaki, M., Tsunemi, H., Inoue, S., Azuma, R., Asahina, Y., Nakamura, S., Kamei, T., Fukuda, M., Asakura, K., Yoshimoto, M., Ode, Y., Hakamata, T., Aoyagi, M., Shima, K., Aoki, Y., Ito, Y., Aoki, D., Fujisawa, K., Shimizu, Y., Higuchi, M., Miyazaki, K., Kusunoki, K., Otsuka, Y., Yokosu, H., Yonemaru, W., Ichikawa, K., Nakano, H., Takemoto, R., Matsushima, T., & Hayashida, K. 2024, in *Society of Photo-Optical Instrumentation Engineers (SPIE) Conference Series*, Vol. 13093, *Space Telescopes and Instrumentation 2024: Ultraviolet to Gamma Ray*, ed. J.-W. A. den Herder, S. Nikzad, & K. Nakazawa, 130931I
- Morris, P. W., Gull, T. R., Hillier, D. J., Barlow, M. J., Royer, P., Nielsen, K., Black, J., & Swinyard, B. 2017, *ApJ*, 842, 79
- Nasa High Energy Astrophysics Science Archive Research Center (Heasarc). 2014, *HEASoft: Unified Release of FTOOLS and XANADU*, *Astrophysics Source Code Library*, record ascl:1408.004
- Pittard, J. M., & Corcoran, M. F. 2002, *A&A*, 383, 636
- Porquet, D., Dubau, J., & Grosso, N. 2010, *SSRv*, 157, 103
- Porter, F. S., Chiao, M. P., Eckart, M. E., Fujimoto, R., Ishisaki, Y., Kelley, R. L., Kilbourne, C. A., Leutenegger, M. A., McCammon, D., Mitsuda, K., Sawada, M., Szymkowiak, A. E., Takei, Y., Tashiro, M., Tsujimoto, M., Watanabe, T., & Yamada, S. 2016, *Journal of Low Temperature Physics*, 184, 498

- Porter, F. S., Kilbourne, C. A., Chiao, M., Cumbee, R., Eckart, M. E., Fujimoto, R., Ishisaki, Y., Kanemaru, Y., Kelley, R. L., Leutenegger, M., Maeda, Y., Mizumoto, M., Sato, K., Sawada, M., Sneiderman, G., Takei, Y., Tsujimoto, M., Uchida, Y., Watanabe, T., & Yamada, S. 2024, in *Society of Photo-Optical Instrumentation Engineers (SPIE) Conference Series*, Vol. 13093, *Space Telescopes and Instrumentation 2024: Ultraviolet to Gamma Ray*, ed. J.-W. A. den Herder, S. Nikzad, & K. Nakazawa, 130931K
- Russell, C. M. P., Corcoran, M. F., Hamaguchi, K., Madura, T. I., Owocki, S. P., & Hillier, D. J. 2016, *MNRAS*, 458, 2275
- Sawada, M., Cumbee, R., de Vries, C., Eckart, M. E., Fujimoto, R., Ishisaki, Y., Kilbourne, C. A., Kitamoto, S., Leutenegger, M. A., Porter, F. S., Shipman, R. F., Takei, Y., & Tsujimoto, M. 2024, in *Society of Photo-Optical Instrumentation Engineers (SPIE) Conference Series*, Vol. 13093, *Space Telescopes and Instrumentation 2024: Ultraviolet to Gamma Ray*, ed. J.-W. A. den Herder, S. Nikzad, & K. Nakazawa, 1309364
- Sekiguchi, A., Tsujimoto, M., Kitamoto, S., Ishida, M., Hamaguchi, K., Mori, H., & Tsuboi, Y. 2009, *PASJ*, 61, 629
- Smith, N. 2006, *ApJ*, 644, 1151
- Smith, N., Gehrz, R. D., Hinz, P. M., Hoffmann, W. F., Hora, J. L., Mamajek, E. E., & Meyer, M. R. 2003, *AJ*, 125, 1458
- Stevens, I. R., Blondin, J. M., & Pollock, A. M. T. 1992, *ApJ*, 386, 265
- Strawn, E., Richardson, N. D., Moffat, A. F. J., Ibrahim, N., Lane, A., Pickett, C., Chené, A.-N., Corcoran, M. F., Damineli, A., Gull, T. R., Hillier, D. J., Morris, P., Pablo, H., Thomas, J. D., Stevens, I. R., Teodoro, M., & Weigelt, G. 2023, *MNRAS*, 519, 5882
- Tashiro, M., Kelley, R., Watanabe, S., Maejima, H., Reichenthal, L., Toda, K., Hartz, L., Santovincenzo, A., Matsushita, K., Yamaguchi, H., Petre, R., Williams, B., Guainazzi, M., Costantini, E., Takei, Y., Ishisaki, Y., Fujimoto, R., Henegar-Leon, J., Sneiderman, G., Tomida, H., Mori, K., Nakajima, H., Terada, Y., Holland, M., Loewenstein, M., Miller, E., Sawada, M., Kallman, T., Kaastra, J., Done, C., Enoto, T., Bamba, A., Corrales, L., Ueda, Y., Kara, E., Zhuravleva, I., Fujita, Y., Arai, Y., Audard, M., Awaki, H., Ballhausen, R., Baluta, C., Bando, N., Behar, E., Bialas, T., Boissay-Malaquin, R., Brenneman, L., Brown, G. V., Chiao, M., Cumbee, R., de Vries, C., den Herder, J.-W., Díaz Trigo, M., DiPirro, M., Dotani, T., Carrero, J. E., Ebisawa, K., Eckart, M., Eckert, D., Eguchi, S., Ezoe, Y., Ferrigno, C., Foster, A., Fukazawa, Y., Fukushima, K., Furuzawa, A., Gallo, L., Garcia Martinez, J., Gortler, N., Grim, M., Gu, L., Hagino, K., Hamaguchi, K., Hatsukade, I., Hayashi, K., Hayashi, T., Hell, N., Hodges-Kluck, E., Horiuchi, T., Hornschemeier, A., Hoshino, A., Ichinohe, Y., Ikuta, C., Iizuka, R., Ishi, D., Ishida, M., Ishihama, N., Ishikawa, K., Ishimura, K., Jaffe, T., Katsuda, S., Kanemaru, Y., Kenyon, S., Kilbourne, C., Kimball, M., Kitamoto, S., Kobayashi, S., Kohmura, T., Kubota, A., Leutenegger, M., Maeda, Y., Markevitch, M., Matsumoto, H., Matsuzaki, K., McCammon, D., McLaughlin, B., McNamara, B., Mernier, F., Miko, J., Miller, J., Minesugi, K., Mitani, S., Mitsuishi, I., Mizumoto, M., Mizuno, T., Mukai, K., Murakami, H., Mushotzky, R., Nakazawa, K., Natsukari, C., Ness, J.-U., Nigo, K., Nishiyama, M., Nobukawa, K., Nobukawa, M., Noda, H., Odaka, H., Ogawa, M., Ogawa, S., Ogorzalek, A., Okajima, T., Okamoto, A., Ota, N., Ozaki, M., Paltani, S., Plucinsky, P., Porter, F. S., Pottschmidt, K., Quero, J. A., Sasaki, T., Sato, K., Sato, R., Sato, T., Sato, Y., Seta, H., Shida, M., Shidatsu, M., Shigeto, S., Shipman, R., Shinozaki, K., Shirron, P., Simionescu, A., Smith, R., Soong, Y., Suzuki, H., Szymkowiak, A., Takahashi, H., Takeo, M., Tamagawa, T., Tamura, K., Tanaka, T., Tanimoto, A., Terashima, Y., Tsuboi, Y., Tsujimoto, M., Tsunemi, H., Tsuru, T., Uchida, H., Uchida, N., Uchida, Y., Uchiyama, H., Uno, S., Vink, J., Witthoef, M., Wolfs, R., Yamada, S., Yamada, S., Yamaoka, K., Yamasaki, N., Yamauchi, M., Yamauchi, S., Yanagase, K., Yaqoob, T., Yasuda, S., Yoneyama, T., Yoshida, T., & Yukita, M. 2025, *PASJ*

- Thompson, A., Lindau, I., Attwood, D., Liu, Y., Gullikson, E., Pianetta, P., Howells, M., Robinson, A., Kim, K.-J., Scofield, J., Kirz, J., Underwood, J., Kortright, J., Williams, G., & Winick, H. 2009, X-ray Data Booklet (Center for X-ray optics and advanced light source, Lawrence Berkeley National Laboratory, University of California)
- Tsuboi, Y., Koyama, K., Sakano, M., & Petre, R. 1997, PASJ, 49, 85
- Usov, V. V. 1992, ApJ, 389, 635
- Vander Meulen, B., Camps, P., Stalevski, M., & Baes, M. 2023, A&A, 674, A123
- Vander Meulen, B., Camps, P., Tsujimoto, M., & Wada, K. 2024, A&A, 688, L33
- Verner, E., Bruhweiler, F., & Gull, T. 2005, ApJ, 624, 973
- Virtanen, P., Gommers, R., Oliphant, T. E., Haberland, M., Reddy, T., Cournapeau, D., Burovski, E., Peterson, P., Weckesser, W., Bright, J., van der Walt, S. J., Brett, M., Wilson, J., Millman, K. J., Mayorov, N., Nelson, A. R. J., Jones, E., Kern, R., Larson, E., Carey, C. J., Polat, İ., Feng, Y., Moore, E. W., VanderPlas, J., Laxalde, D., Perktold, J., Cimrman, R., Henriksen, I., Quintero, E. A., Harris, C. R., Archibald, A. M., Ribeiro, A. H., Pedregosa, F., van Mulbregt, P., & SciPy 1.0 Contributors. 2020, Nature Methods, 17, 261
- Yamaguchi, H., Eriksen, K. A., Badenes, C., Hughes, J. P., Brickhouse, N. S., Foster, A. R., Patnaude, D. J., Petre, R., Slane, P. O., & Smith, R. K. 2014, ApJ, 780, 136
- Yoshida, T., Fukushima, K., Hayashi, K., Kanemaru, Y., Ogawa, S., Audard, M., Behar, E., Inoue, S., Ishihara, Y., Kohmura, T., Maeda, Y., Mizumoto, M., Nobukawa, M., Pottschmidt, K., Shidatsu, M., Terada, Y., Terashima, Y., Tsuboi, Y., Uchida, H., Yoneyama, T., & Yoshimoto, M. 2024, The Astronomer's Telegram, 16652, 1